

# The Growth of Sodic Amphibole at the Greenschist-to Blueschist-facies Transition (Dent Blanche, Western Alps): Bulk-rock Chemical Control and Thermodynamic Modelling

Paola Manzotti, Michel Ballèvre, Pavel Pitra, Benita Putlitz, Martin Robyr, Othmar Mü Ntener

▶ **To cite this version:**

Paola Manzotti, Michel Ballèvre, Pavel Pitra, Benita Putlitz, Martin Robyr, et al.. The Growth of Sodic Amphibole at the Greenschist-to Blueschist-facies Transition (Dent Blanche, Western Alps): Bulk-rock Chemical Control and Thermodynamic Modelling. Journal of Petrology, 2020, 61 (4), pp.egaa044. 10.1093/petrology/egaa044 . insu-02879619

**HAL Id: insu-02879619**

**https://insu.hal.science/insu-02879619**

Submitted on 29 Sep 2020

**HAL** is a multi-disciplinary open access archive for the deposit and dissemination of scientific research documents, whether they are published or not. The documents may come from teaching and research institutions in France or abroad, or from public or private research centers.

L'archive ouverte pluridisciplinaire **HAL**, est destinée au dépôt et à la diffusion de documents scientifiques de niveau recherche, publiés ou non, émanant des établissements d'enseignement et de recherche français ou étrangers, des laboratoires publics ou privés.



Distributed under a Creative Commons Attribution 4.0 International License

JOURNAL OF PETROLOGY

*Journal of Petrology*, 2020, 1–30
doi: 10.1093/petrology/egaa044
Advance Access Publication Date: 20 March 2020
Original Manuscript

OXFORD

# The Growth of Sodic Amphibole at the Greenschist- to Blueschist-facies Transition (Dent Blanche, Western Alps): Bulk-rock Chemical Control and Thermodynamic Modelling

**Paola Manzotti [1,2]*, Michel Ballèvre[3], Pavel Pitra[3,4], Benita Putlitz[2], Martin Robyr[2] and Othmar Müntener[2]**

[1]Department of Geological Sciences, Stockholm University, Stockholm 106 91, Sweden; [2]Institute of Earth Sciences, University of Lausanne, Géopolis, Quartier Mouline, 1015 Lausanne, Switzerland; [3]Université Rennes 1, CNRS, Géosciences Rennes-UMR 6118, F-35000 Rennes, France; [4]Česká geologická služba, Prague 1, Czech Republic

*Corresponding author. Telephone: +46 (0)8 16 4745. E-mail: paola.manzotti@geo.su.se

## ABSTRACT

The sodic amphibole glaucophane is generally considered as indicative of blueschist-facies metamorphism. However, sodic amphiboles display a large range in chemical compositions, owing principally to the $Fe^{2+}Mg_{-1}$ and $Fe^{3+}Al_{-1}$ substitutions. Therefore, the whole-rock composition (namely its $Na_2O$ and FeO* content, and the $Fe^{2+}$–$Fe^{3+}$ ratio), strongly controls the stability field of the sodic amphiboles at the transition from greenschist- to blueschist-facies conditions. Neglecting these variables can lead to erroneous estimates of the metamorphic conditions and consequently the tectonic framework of the rocks. This paper explores the mechanisms that control the development of sodic amphibole and sodic pyroxene within the basement of the Dent Blanche Tectonic System (Western Alps), as a result of the Alpine metamorphic history. Field, petrographic and geochemical data indicate that sodic amphibole and sodic pyroxene form in different rock types: (1) in undeformed pods of ultramafic cumulates (hornblendite), sodic amphibole (magnesioriebeckite) forms coronas around magmatic pargasite; (2) metatonalite displays patches of radiating sodic (magnesioriebeckite) and calcic (actinolite) amphiboles; (3) sodic amphibole (magnesioriebeckite–glaucophane) occurs with high-Si potassic white mica (phengitic muscovite) in fine-grained (blue) schists; (4) in mylonitized granitoids (amphibole-gneiss) metasomatized along the contact with ultramafic cumulates, sodic amphibole (magnesioriebeckite–winchite) mainly forms rosettes or sheaves, generally without a shape-preferred orientation. Only locally are the needles aligned parallel to the stretching lineation. Pale green aegirine–augite is dispersed in an albite–quartz matrix or forms layers of fine-grained fibrous aggregates. The bulk-rock chemical composition of the different lithologies indicates that sodic amphibole and sodic pyroxene developed in Na- and Fe-rich systems or in a system with high $Fe^{3+}$/Fe*. Thermodynamic modelling performed for different rock types (taking into account the measured $Fe_2O_3$ contents) reveals that sodic amphibole appears at $\sim 8 \pm 1$ kbar and 400–450 °C (i.e. at the transition between the greenschist- and blueschist-facies conditions) about 5 kbar lower than previous estimates. To test the robustness of our conclusion, we performed a review of sodic amphibole compositions from a variety of terranes and *P*–*T* conditions. This shows (1) systematic variations of composition with *P*–*T* conditions and bulk-rock chemistry, and (2) that the amphibole compositions reported from the studied area are consistent with those reported from other greenschist- to blueschist-facies transitions.

**Key words:** *sodic amphibole*; *$Fe^{3+}$*; *blueschist–greenschist*; *Dent Blanche*; *Alps*

© The Author(s) 2020. Published by Oxford University Press.
This is an Open Access article distributed under the terms of the Creative Commons Attribution License (http://creativecommons.org/licenses/by/4.0/), which permits unrestricted reuse, distribution, and reproduction in any medium, provided the original work is properly cited.



Downloaded from https://academic.oup.com/petrology/advance-article/doi/10.1093/petrology/egaa044/5810502 by guest on 29 September 2020

## INTRODUCTION

The sodic amphibole glaucophane is an iconic mineral, because of the attractive blue colour, and because it classically defines the blueschist facies. Because glaucophane may occur in a wide range of bulk-rock compositions, its use for assessing pressure–temperature (*P*–*T*) conditions (e.g. Evans & Brown, 1986; Bucher & Grapes, 2011) requires great care in multicomponent chemical systems where the number of components exceeds the number of phases. Sodic amphiboles, with the generalized chemical formula $\square Na_2(Mg,Fe_{2+})3(Al,Fe_{3+})Si_8O_22(OH)2$ (where $\square$ represents a vacancy), display a wide range of compositions, among others owing to the substitutions of divalent as well as trivalent cations. Iron can occur in both di- and trivalent states, and the transition from the greenschist to the blueschist facies is therefore very sensitive to the oxidation state of the rock (i.e. to the ratio of $Fe^{2+}$ and $Fe^{3+}$), in addition to the bulk-rock Na content. This has been clearly shown on an empirical basis by Miyashiro & Banno (1958) and Brown (1974, 1977). Further theoretical development by Liou *et al.* (1985) and experimental data by Maruyama *et al.* (1986) have definitely established this point.

With the advent of thermodynamic databases, the shift of the metamorphic facies boundaries, based on the presence of a sodic amphibole in a model system for metabasite, has been calculated by Evans (1990) (Fig. 1), and later confirmed by many others calculating phase diagrams for specific bulk-rock compositions (e.g. White *et al.*, 2000, 2002; Fitzherbert *et al.*, 2003, 2005; Warren & Waters, 2006; Diener *et al.*, 2007; Groppo *et al.*, 2009*a*; Diener & Powell, 2010; López-Carmona *et al.*, 2013). For example, Diener & Powell (2010) have shown that for a model mid-ocean ridge basalt (MORB) composition at 450 °C, the first appearance of glaucophane occurs at ~9·3 kbar in an $Fe^{3+}$-free system, but that *P* decreases to ~5·5 kbar with increasing $Fe^{3+}$ content for a given, constant, total amount of Fe.

Despite these caveats, sodic amphibole is considered an important indicator of high-*P*, low-*T* conditions, and is often interpreted as relic of blueschist-facies metamorphism. However, without a proper chemical characterization of the sodic amphibole, *P*–*T* evaluations may be uncertain. An excellent example is provided by the Dent Blanche Tectonic System (DBTS) in the Western Alps (Fig. 2), where reports of sodic amphibole (e.g. Diehl, 1938; Stutz, 1940; Diehl *et al.*, 1952; Ayrton *et al.*, 1982; Roda & Zucali, 2008; Angiboust *et al.*, 2014) have been taken for a long time as indicative of an early blueschist-facies stage (e.g. Oberhänsli *et al.*, 2004; Berger & Bousquet, 2008; Beltrando *et al.*, 2010; Bousquet *et al.*, 2012). The scarce occurrence of sodic amphibole, and its peculiar $Fe^{3+}$-rich chemistry (Ballèvre & Kienast, 1987; Canepa *et al.*, 1990; Roda & Zucali, 2008; Manzotti *et al.*, 2012, 2014*a*), may be explained by two different hypotheses.

The first hypothesis is that the *P*–*T* path of the DBTS may have reached the blueschist facies, but the blueschist-facies parageneses have been preserved in only a limited number of rocks because of the extensive greenschist-facies overprint (path A in Fig. 1; Roda & Zucali, 2008; Angiboust *et al.*, 2014). The second hypothesis is that the rocks may have reached much lower *P*, at the transition between greenschist and blueschist facies (Ballèvre & Kienast, 1987) (consistent with path B in Fig. 1). In this hypothesis, the development of sodic amphibole may have been limited to specific bulk-rock chemistries (e.g. Na-rich, Fe-rich or high $fO_2$).

In this paper, we test these two hypotheses. Following an extensive mapping campaign (Manzotti & Ballèvre, 2017; Manzotti *et al.*, 2017), we studied the rare sodic amphibole-bearing rocks as well as a much larger number of samples that do not contain sodic amphibole. This allows us to determine the chemistry of both the amphibole and the bulk-rocks in which it occurs (or not), a prerequisite for attempting to model the relevant phase diagrams. The goal of the thermodynamic modelling is primarily the qualitative understanding of the behaviour of Na-amphibole at the greenschist–blueschist-facies transition in various rock types, rather than the determination of precise *P*–*T* conditions of the DBTS. We show that the sodic amphibole develops in a variety of rock types, including metasomatic layers at the contact between ultramafic

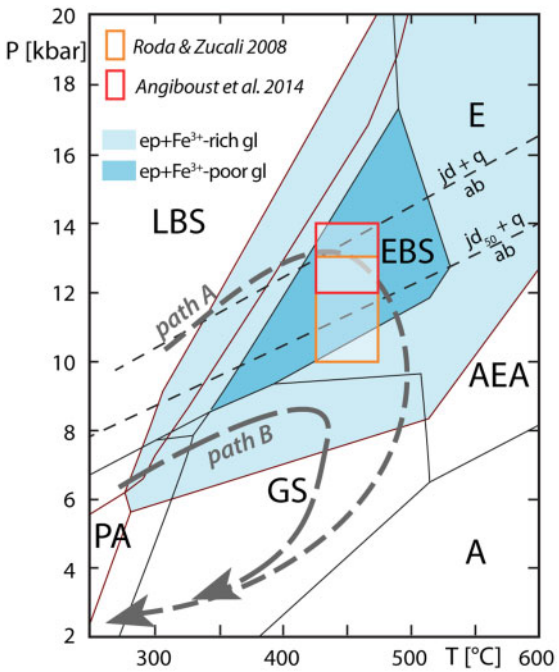



**Fig. 1.** Two possible *P*–*T* paths for the DBTS (Western Alps). Peak metamorphic conditions estimated in previous studies are reported (red and orange rectangles). Light and dark blue fields in the *P*–*T* diagram refer to the epidote blueschist-facies stability field calculated using two different compositions of sodic amphiboles, rich and poor in $Fe^{3+}$ respectively (Evans, 1990). EBS, epidote-blueschist; LBS, lawsonite-blueschist; AEA, albite–epidote-amphibolite; A, amphibolite; E, eclogite; GS, greenschist; PA, pumpellyite–actinolite.

Downloaded from https://academic.oup.com/petrology/advance-article/doi/10.1093/petrology/egaa044/5810502 by guest on 29 September 2020

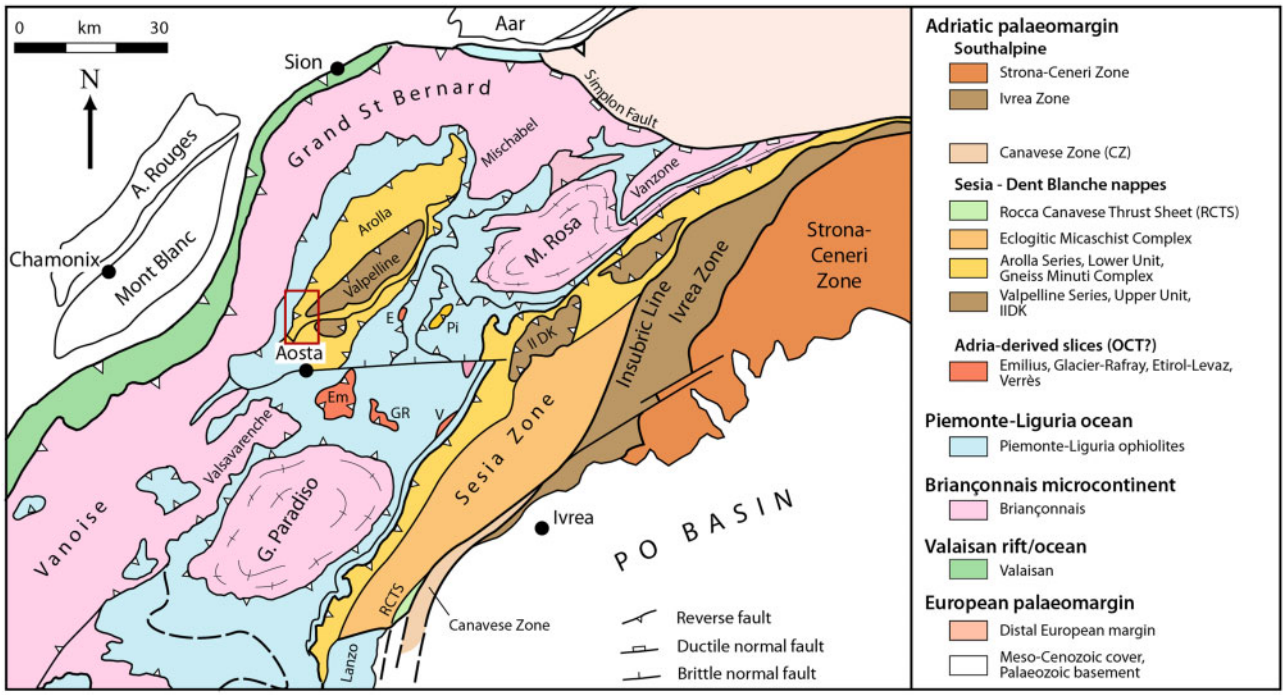



**Fig. 2.** Simplified structural map of the North Western Alps (modified after Manzotti *et al.*, 2014*a*, 2014*b*). The studied samples are from the frontal part of the Dent Blanche Tectonic System, north of Aosta (see red rectangle). Further details on the location of the samples may be found in Table 1 and in the Supplementary Data (Fig. S1).

cumulates and orthogneisses, at relatively low *P*; that is, at the transition from the greenschist to the blueschist facies.

## GEOLOGICAL SETTING

### The Dent Blanche Tectonic System

The internal Western Alps comprise continental and oceanic units, which were assembled during the oblique convergence of Europe and the thinned Adriatic margin (Schmid *et al.*, 2004; Handy *et al.*, 2010). The Dent Blanche Tectonic System (DBTS) was derived from the Adriatic palaeomargin and, together with the Sesia Zone (Fig. 2), forms the Sesia–Dent Blanche nappes (e.g. Manzotti *et al.*, 2014*b*, 2017). The DBTS mainly comprises polycyclic basement slices, bounded by Alpine shear zones (Manzotti *et al.*, 2014*a*). The tectonometamorphic setting of the DBTS has been described in previous studies (e.g. Manzotti *et al.*, 2014*b*, 2017). Therefore, only the structural and metamorphic features relevant for this study are hereafter summarized. The DBTS is made of two basement nappes, the Dent Blanche (DB) and the Mont Mary Cervino (MM) (see Manzotti *et al.*, 2017, fig. 1), which are separated by the crustal-scale Roisan–Cignana Shear Zone (RCSZ; Manzotti, 2011; Manzotti *et al.*, 2014*a*). Mesozoic metasediments deposited on top of the Palaeozoic basement are preserved in the Mont Dolin Series (Weidmann & Zaninetti, 1974; Ayrton *et al.*, 1982) and the Roisan Zone (Manzotti *et al.*, 2014*b*; Ciarapica *et al.*, 2016).

The Valpelline Series in the DB and the Upper Unit in the MM are slivers of Permian lower continental crust and mainly consist of amphibolite- to granulite-facies metapelites, and mafic and metacarbonate rocks (Gardien *et al.*, 1994; Manzotti & Zucali, 2013; Dal Piaz *et al.*, 2015; Kunz *et al.*, 2018). The Arolla Series of the DB comprises Permian granitoids (e.g. Diehl *et al.*, 1952; Roda & Zucali, 2008; Manzotti *et al.*, 2018) and gabbros (e.g. Dal Piaz *et al.*, 1977; Monjoie *et al.*, 2007; Baletti *et al.*, 2012; Manzotti *et al.*, 2017) and their metamorphic products. The Lower Unit of the MM consists of pre-Alpine amphibolite-facies metapelites and minor granitoids, leucocratic gneisses and pegmatites (Canepa *et al.*, 1990; Dal Piaz *et al.*, 2010; Manzotti *et al.*, 2014*a*).

### Alpine metamorphism in the DBTS

Alpine greenschist-facies metamorphism is dominant in the DBTS (e.g. Ayrton *et al.*, 1982). However, a few occurrences of sodic amphibole and sodic pyroxene may indicate early, blueschist-facies, metamorphism. For instance, metamorphic assemblages comprising sodic pyroxene and/or sodic amphibole have been described in the meta-igneous rocks, of acid, intermediate and basic compositions and in Mesozoic metasediments (see Supplementary Data Table S1 and references therein; Supplementary Data are available for downloading at http://www.petrology.oxfordjournals.org).

Out of 17 studies, the bulk chemistry of the sodic amphibole-bearing rocks has been analysed in only two cases and the chemistry of sodic amphibole in five

Downloaded from https://academic.oup.com/petrology/advance-article/doi/10.1093/petrology/egaa044/5810502 by guest on 29 September 2020

**Table 1:** Compilation of geographical coordinates and main petrographical characters of the studied samples

| Site | GPS coordinates | Rock type | Sample name | Preserved magmatic relics | Metamorphic minerals | |
|---|---|---|---|---|---|---|
| | | | | | Silicates | Non-silicates |
| 1 | 45°53′13·29"N, 7°21′02·35"E | hornblendite | OL02* | am (hb–prg–ed)–Ti mt–ilm | Type 1: mrbk to wnc–ep–chl–ab–q–ttn; Type 2: ep–act–chl | ru–py–hem |
| | | hornblendite | OL03† | am (hb–prg–ed)–Ti mt–ilm | Type 1: mrbk to wnc–ep–chl–ab–q–ttn; Type 2: ep–act–chl | ru–py–hem |
| | | hornblendite | OL04† | am (hb–prg–ed)–Ti mt–ilm | Type 1: mrbk to wnc–ep–chl–ab–q–ttn; Type 2: ep–act–chl | ru–py–hem |
| 2 | 45°52′25·37"N, 7°20′28·71"E | orthogneiss | OL25‡ | kfs–aln–zrn | q–ab–ep–mu–chl–ttn | py–hem |
| | | orthogneiss | OL24‡ | kfs–aln–zrn | q–ab–ep–mu–chl–ttn | py–hem |
| | | orthogneiss | OL23‡ | kfs–aln–zrn | q–ab–ep–mu–chl–ttn | hem |
| | | am-gneiss | OL50‡ | aln–zrn | q–ab–ep–mrbk–wnc–act | — |
| | | am-gneiss | OL68A† | aln–zrn | q–ab–ep–ttn | mt–hem–py |
| | | am-gneiss | OL68B* | aln–zrn | q–ab–ep–mrbk–wnc–act–aeg–aug–ttn | mt–hem |
| | | am-gneiss | OL49C‡ | aln–zrn | q–ab–ep–chl | — |
| | | mu-rich layer | OL49B‡ | Zrn | mu–ep | — |
| | | chl-schist | OL49A‡ | aln–zrn–ap | chl–ep±mu | — |
| | 45°52′24·37"N, 7°20′28·71"E | ultramafic | OL35† | — | srp–Mg-chl–tr–ttn | cal–mt |
| | | ultramafic | OL34† | — | srp–Mg-chl–tr–ttn | cal–mt |
| | | ultramafic | OL33† | — | srp–Mg-chl–tr–ttn–tlc | cal–mt |
| 3 | 45°52′26·78"N, 7°20′25·97"E | am-gneiss | OL61‡ | zrn–aln | q–ab–ep–mrbk–wnc–act | Py |
| | | | OL62† | zrn–aln | q–ab–ep–mrbk–wnc–act–ttn | — |
| | | | OL63† | zrn–aln | q–ab–ep–mrbk–wnc–act–ttn | — |
| 4 | 45°52′27·29"N, 7°20′16·57"E | am-gneiss | OL21† | zrn–aln | q–ab–ep–mrbk–wnc–act | py |
| | 45°52′25·76"N, 7°20′24·64"E | ultramafic | OL60† | — | srp–Mg-chl–tr–ttn | cal–mt |
| 5 | 45°52′08·39"N, 7°19′44·77"E | am-gneiss | OL06† | aln–zrn | q–ab–ep–mrbk–wnc–act–ttn | py |
| | | orthogneiss | OL08‡ | kfs–aln–zrn | q–ab–ep–mu–chl–ttn | — |
| | 45°52′13·58"N, 7°19′49·29"E | metagabbro | OL1424* | | mu–zo–Mg-chl | — |
| 6 | 45°51′43·82"N, 7°19′35·02"E | meta-tonalite | OL39† | zrn–aln–mnz–mu–q | q–ab–mrbk–wncaeg–aug–ep–ttn | py |
| | | | OL40‡ | zrn–aln–mnz–mu–q | q–ab–mrbk–wnc–aeg–aug–ep–ttn | — |
| | | | OL43* | zrn–aln–mnz–mu–q | q–ab–mrbk–wnc–act–aeg–aug–ep–ttn | — |
| | | | OL44† | zrn–aln–mnz–mu | q–ab–mrbk–wnc–aeg–aug–ep–ttn | py |
| | | meta-tonalite | OL42A† | zrn–aln–mnz–q | q–ab–mrbk–chl | — |
| | 45°51′43·82"N, 7°19′35·02"E | chl-schist | OL42B‡ | zrn–ap–mnz | Mg-chl | — |
| | | ultramafic | OL54† | — | srp–Mg-chl–ttn | mt |
| | | ultramafic | OL55† | — | srp–mt | mt |
| 7 | 45°47′13·38"N, 7°19′01·57"E | blueschist | VP7* | zrn–aln–ap | gl–mrbk–mu–ep–chl–ttn–q–g | py |
| | M. Morion (Diehl *et al.* 1952) | orthogneiss | 14§ | | q–ab–ep–mu–chl–ttn | — |

*Whole-rock chemistry + microprobe + thermodynamic modelling.
†Whole-rock chemistry.
‡Whole-rock chemistry + microprobe.
§Thermodynamic modelling.



Downloaded from https://academic.oup.com/petrology/advance-article/doi/10.1093/petrology/egaa044/5810502 by guest on 29 September 2020

cases only (Table S1), indicating mostly magnesioriebeckite and rarely glaucophane. Although some researchers described aegirine–augite in the DBTS (e.g. De Leo *et al.*, 1987; Pennacchioni & Guermani, 1993), not a single chemical analysis of sodic pyroxene has been reported.

For the Arolla orthogneisses, peak *P*–*T* conditions of 12–14 kbar and ~450 °C have been estimated on the basis of conventional thermobarometry and phase equilibria (e.g. Roda & Zucali, 2008). A pseudosection approach has been used to constrain peak and retrograde evolution of Arolla orthogneisses devoid of sodic amphibole (Angiboust *et al.*, 2014; Kirst, 2017), and it returned similar *P*–*T* conditions. For the Lower Unit of the Mont Mary, thermobarometric calculations have provided an estimate at 13 ± 2 kbar and 480 ± 50 °C (Manzotti *et al.*, 2014*a*).

## METHODS

Out of a collection of a few hundred samples from the DBTS, we found 16 samples from seven localities in which sodic amphibole and/or sodic pyroxene have been observed (Figs 3 and 4, Table 1, Supplementary Data Fig. S1). The bulk-rock composition of all these samples has been analysed (with the exception of sample OL44, because it was too altered) and the mineral chemistry has been determined in detail in eight samples. Our study also includes 14 samples that do not contain sodic amphibole and/or pyroxene (Table 1). The bulk-rock chemistry has been obtained for the entire set of samples and the mineral chemistry has been studied in detail in six samples. Thermodynamic modelling has been applied on six samples, four of which contain sodic amphibole and/or sodic pyroxene, and two of which are devoid of these minerals. The variety of rock types and provenance of the selected samples allow us to evaluate the geochemical control (protolith bulk composition versus successive fluid-rock interactions) on the development of sodic amphibole and pyroxene.

### Mineral chemistry

Samples were investigated by optical petrography in polished thin sections (Fig. 5) and back-scattered electron (BSE) imaging by scanning electron microscopy. Mineral abbreviations and symbols used in this study are listed in Supplementary Data Table S2. For practical purpose, muscovite is used for potassic white mica, whatever its Si content, because there is no formal definition of phengite and because there is no miscibility gap between muscovite and celadonite.

A JEOL JXA-8530F electron probe microanalyzer at the Institute of Earth Science of the University of Lausanne (Switzerland) was used to acquire quantitative analyses of mineral phases and X-ray compositional maps in wavelength-dispersive mode. Spot analyses were performed using an accelerating voltage of 15 keV. A current of 20 nA was used for garnet and clinopyroxene spot analysis. To avoid electron-beam-induced decomposition of minerals containing volatile elements, a current of 15 nA was applied for plagioclase, amphibole, chlorite, muscovite and epidote quantitative measurements. For these latter phases, a beam size ranging between 2 and 5 μm was used depending on the size of the mineral. The X-ray compositional mapping was carried out at 50 ms on 0·7 μm pixel, using an acceleration voltage of 15 keV and a current of 20 nA.

To evaluate the oxidation state of the studied samples, the oxide minerals present (magnetite and hematite) were identified optically and confirmed by Raman spectroscopy (Horiba HR Raman-FTIR spectrometer from HORIBA Scientific, an integrated Raman microprobe consisting of an Olympus BX41 confocal microscope coupled to an 800 mm focal-length spectrograph, Institute of Earth Sciences, University of Lausanne).

Because the microprobe analyses do not readily distinguish $Fe^{2+}$ and $Fe^{3+}$, and because this is a fundamental aspect of our study, the procedure followed is explained in more detail below. In pyroxene, the $Fe^{3+}$ content has been calculated by stoichiometry. Structural formulae for this mineral have been calculated on the basis of six oxygens and four cations. The recalculation procedure for amphibole has been discussed in detail by Schumacher (1997, 2007). For each analysis, a minimum, a maximum (and a mean) estimation of the $Fe^{3+}$ can be obtained. The influence of using one (or the other) calculation scheme is displayed for some analyses in Figure 6 [i.e. the diagram proposed by Miyashiro & Banno (1958) and adopted later in the classification of sodic amphiboles, except for crossite (Leake *et al.*, 1997)]. Specifically, we reported as large symbols the recalculation giving the maximum amount of $Fe^{3+}$ [generally on O = 23 and sum of cations except Ca, Na, K = 13 for sodic amphiboles; see Schumacher (2007)], and the two other estimations (i.e. the minimum and the mean) are plotted in the classification diagram as a thin line joining the highest estimate to the two other ones (Fig. 6). For consistency, we plotted all amphibole analyses with a maximum amount of $Fe^{3+}$. This has some influence on their position in the diagram, but the uncertainty introduced by the recalculation scheme is negligible (i.e. very short lines) in most cases or moderate for a few cases. Some amphibole analyses may fall into different fields according to which calculation scheme is adopted. However, because there is no miscibility gap between the different end-members plotted in Miyashiro's diagram, the important point is not the name of the amphibole (the different fields have arbitrary limits), but the location of the analyses in the diagram, whichever of the four fields they fall in.

Representative mineral analyses are reported in the Supplementary Data (Tables S3–S10). The main chemical characteristics of sodic amphibole and sodic pyroxene are given in Table 2.

Downloaded from https://academic.oup.com/petrology/advance-article/doi/10.1093/petrology/egaa044/5810502 by guest on 29 September 2020

**Table 2:** Main chemical characters (major element compositions) of amphibole and pyroxene

| | Sample | Mineral | Si | $(Na + K)_A$ | $X_{Na}$ | $Na_B$ | $X_{Fe}$ | $X_{Fe3}$ | *n* |
|---|---|---|---|---|---|---|---|---|---|
| Hornblendite | OL02 | Prg | 6·39–6·48 | 0·50–0·61 | 0·20–0·22 | | 0·29–0·35 | 0·00–0·05 | 15 |
| | | Ed | 6·55–7·53 | 0·39–0·54 | 0·23–0·37 | | 0·36–0·42 | — | 4 |
| | | Mg-hb | 6·84–7·32 | 0·17–0·49 | 0·21–0·24 | | 0·28–0·48 | 0·09–0·32 | 5 |
| | | mrbk | 7·93–8·00 | 0·00–0·03 | 0·75–0·91 | 1·51–1·82 | 0·38–0·46 | 0·64–0·71 | 10 |
| | | wnc | 7·53–7·97 | 0·00–0·04 | 0·23–0·75 | 0·53–1·49 | 0·27–0·46 | 0·41–0·72 | 34 |
| | | act | 7·65–7·98 | 0·00–0·07 | 0·07–0·26 | | 0·24–0·37 | 0–0·70 | 25 |
| Metatonalite | OL40 | mrbk | 7·90–8·00 | 0·00–0·02 | 0·76–0·97 | 1·53–1·94 | 0·15–0·43 | 0·46–0·87 | 61 |
| | | wnc | 7·90–8·00 | 0·00–0·02 | 0·26–0·74 | 0·55–1·49 | 0·22–0·35 | 0·62–0·87 | 10 |
| | OL42 | wnc | 7·86–8·00 | 0·06–0·16 | 0·18–0·52 | 0·53–1·14 | 0·20–0·27 | 0·00–0·63 | 6 |
| | OL43 | mrbk | 7·94–8·00 | 0·00–0·03 | 0·75–0·97 | 1·51–1·93 | 0·26–0·44 | 0·58–0·73 | 19 |
| | | wnc | 7·87–8·00 | 0·00–0·04 | 0·27–0·74 | 0·51–1·48 | 0·24–0·40 | 0·57–0·72 | 21 |
| | | act | 7·89–8·00 | 0·00–0·01 | 0·04–0·25 | | 0·24–0·35 | 0–0·55 | 20 |
| | OL44 | mrbk | 7·83–7·99 | 0·00–0·04 | 0·75–0·90 | 1·51–1·79 | 0·31–0·42 | 0·52–0·68 | 36 |
| | | wnc | 7·64–7·98 | 0·00–0·11 | 0·22–0·77 | 0·54–1·48 | 0·21–0·44 | 0·42–0·70 | 32 |
| Blueschist | VP7 | gl | 7·87–8·00 | 0·00–0·07 | 0·94–0·99 | 1·87–1·98 | 0·39–0·50 | 0·22–0·50 | 42 |
| | | mrbk | 7·11–8·00 | 0·00–0·08 | 0·87–0·97 | 1·73–1·94 | 0·27–0·51 | 0·45–0·68 | 29 |
| Am-gneiss | OL50 | gl | 7·98–7·99 | 0·00–0·01 | 0·95–0·96 | 1·90–1·92 | 0·37–0·38 | 0·45–0·49 | 5 |
| | | mrbk | 7·93–8·00 | 0·00–0·04 | 0·80–0·95 | 1·60–1·89 | 0·32–0·39 | 0·52–0·64 | 7 |
| | | wnc | 7·75–7·96 | 0·01–0·05 | 0·28–0·69 | 0·55–1·39 | 0·25–0·32 | 0·62–0·72 | 34 |
| | | act | 7·81–7·90 | 0·01–0·03 | 0·12–0·22 | | 0·24–0·30 | 0·51–0·70 | 8 |
| | OL61 | mrbk | 7·94 | 0·00 | 0·85 | 1·60 | 0·44 | 0·62 | 1 |
| | | wnc | 7·84–7·99 | 0·00–0·06 | 0·21–0·65 | 0·51–1·30 | 0·20–0·37 | 0·45–0·72 | 55 |
| | | act | 7·75–7·95 | 0·00–0·04 | 0·15–0·24 | | 0·18–0·43 | 0·51–0·68 | 8 |
| | OL68 | gl | 7·81–7·99 | 0·00 | 0·87–0·98 | 1·74–1·96 | 0·31–0·40 | 0·36–0·47 | 6 |
| | | mrbk | 7·79–7·97 | 0·00–0·12 | 0·65–0·96 | 1·56–1·91 | 0·22–0·41 | 0·48–0·74 | 20 |
| | | wnc | 7·50–7·93 | 0·00–0·19 | 0·30–0·86 | 0·52–1·74 | 0·19–0·51 | 0·27–0·73 | 23 |
| | | act | 7·85–8·00 | 0·03–0·17 | 0·11–0·29 | | 0·40–0·54 | — | 10 |
| | Sample | Mineral | Jd | Aeg | *n* | | | | |
| Metatonalite | OL43 | aeg–aug | 0·13–0·26 | 0·30–0·42 | 58 | | | | |
| | OL44 | aeg–aug | 0·04–0·34 | 0·23–0·44 | 75 | | | | |
| Am-gneiss | OL68 | aeg–aug | 0·07–0·24 | 0·29–0·43 | 30 | | | | |

$X_{Na} = Na/(Na + Ca)$; $X_{Fe} = Fe^{2+}/(Fe^{2+} + Mg)$; $X_{Fe3} = Fe^{3+}/(Fe^{3+} + Al)$; *n*, number of analyses.

## Bulk-rock chemistry

To assess the nature and the degree of chemical modification in the rocks displaying sodic amphibole and/or sodic pyroxene in the DBTS, we analysed the major and trace element compositions of the selected set of samples (Table 4 and Tables S11–S16). We performed two or three separate bulk-rock analyses for samples that macroscopically showed different domains (e.g. OL49), to obtain the most representative chemical composition of each domain. Major elements were determined by inductively coupled plasma atomic emission spectrometry (ICP-AES; SARM-CRPG, Nancy). Bulk-rock glasses were fused at 980 °C by mixing appropriate proportions (1 %) of fine-grained rock powder with di-lithium tetraborate. Then, glasses were dissolved in a mixture of $HNO_3$ (5 %), $H_2O_2$ (0·5 %) and glycerol (10 %) prior to analysis. Details about the method used for the analyses have been given by Carignan *et al.* (2001). Uncertainties at 1σ are *c.* 5 % for the ICP-AES data. In addition, separate analyses of $Fe^{2+}$ content of whole-rock samples were performed (SARM-CRPG, Nancy, France) by titration with potassium dichromate after dissolution of the sample in a $HF–H_2SO_4$ mixture, in the presence of $H_3BO_3$ and $H_3PO_4$.

## Phase diagram calculations

*P–T* pseudosections were calculated with Theriak/Domino (de Capitani & Brown, 1987; de Capitani & Petrakakis, 2010), the internally consistent thermodynamic dataset ds6.2 (Holland & Powell, 2011) and mixing models for solid solutions (converted for Theriak/Domino by D. K. Tinkham, http://dtinkham.net/peq.html).

Phase relations were modelled in the chemical system $Na_2O–CaO–FeO–MgO–Al_2O_3–SiO_2–H_2O–TiO_2–Fe_2O_3 \pm MnO \pm K_2O$ (MnNCKFMASHTO). In the first step, $H_2O$ was considered in excess in all calculations. The phases considered in the calculations and the activity composition models are clinoamphibole and clinopyroxene (Green *et al.*, 2016), chlorite, muscovite, garnet, biotite (White *et al.*, 2014*a*, 2014*b*), plagioclase (Holland & Powell, 2003), epidote (Holland & Powell, 2011), ilmenite (White *et al.*, 2000), magnetite (White *et al.*, 2002), pumpellyite (ideal mixing on sites). Pure phases comprise quartz, titanite, and rutile. The activity–composition (*a–x*) relations (i.e. White *et al.*, 2014*a*, 2014*b*) used with the internally consistent thermodynamic dataset of Holland & Powell (2011) include $Fe^{3+}$ in several silicate phases (e.g. garnet, chlorite, biotite, staurolite, chloritoid, muscovite, paragonite, and margarite).

*P–T* pseudosections were calculated using the amount of $Fe^{2+}$ (versus $Fe^{3+}$) measured in the bulk composition. As rocks can be affected by surface weathering processes including oxidation, the measured amount of $Fe^{3+}$ is considered as the maximum value on

Downloaded from https://academic.oup.com/petrology/advance-article/doi/10.1093/petrology/egaa044/5810502 by guest on 29 September 2020

the range of possible $Fe^{3+}$ contents (Diener & Powell, 2010). *P*–*X*($Fe_2O_3$) (expressed in wt%) pseudosections were calculated to explore the effect of variable $Fe^{2+}$/$Fe^{3+}$ ratio in the bulk-rock. In these calculations, *T* was generally fixed at 450 °C, a value that, according to previous studies (e.g. Roda & Zucali, 2008; Angiboust *et al.*, 2014; Kirst, 2017) corresponds to the *T* reached by the DBTS at peak *P* conditions. In the diagrams, the abbreviation 'gl' has been used for sodic amphibole, whereas clinopyroxene is indicated with the abbreviation 'cpx'.

*P*–$H_2O$ (expressed in wt%) diagrams were calculated to explore the effect of variable bulk-rock $H_2O$ on phase equilibria and *P*–*T* estimates. These diagrams were constructed for the same bulk compositions as used for the *P*–*T* diagrams (Fig. 14d and Figs S4–S5), for a *T* of 450 °C and a *P* range of 4–12 kbar.

## PETROGRAPHY AND MINERAL CHEMISTRY

In the DBTS, the dominant rock types are felsic orthogneisses of granitic to dioritic composition (the Arolla orthogneisses), paragneisses interpreted as the country-rocks of these intrusions (Manzotti *et al.*, 2018), and a few metagabbroic complexes, displaying ultramafic cumulates, and mesocratic and leucocratic metagabbro (e.g. the Berrio Gabbro, Manzotti *et al.*, 2017). All these rock types are devoid of sodic amphibole and sodic pyroxene. These two minerals are, however, found in minor rock types that belong to two main groups. The first one does not show obvious signs of metasomatism and comprises (1) a single occurrence of hornblendite in the Berrio Gabbro, (2) a few metatonalite pods within ultramafic cumulates from the Berrio Gabbro, and (3) rare blueschists interlayered with felsic orthogneisses (Manzotti *et al.*, 2014*a*). The second group consists of amphibole-gneisses, located in reaction zones, at the boundary between the Arolla orthogneisses and the ultramafic cumulates of the Berrio Gabbro (Figs 3 and 4). These four types of rocks are described in more detail below. For comparison, we also studied in detail two rocks that contain neither sodic amphibole nor sodic pyroxene; namely, a leucocratic metagabbro and an Arolla orthogneiss.

### Hornblendite lenses in the Berrio Gabbro

Decametre-long lenses of unfoliated hornblendite are found included in the mylonitic Berrio metagabbro (Supplementary Data, Fig. S1). Based on differences in their mineral assemblages, two domains may be distinguished at the microscale. The type-I domain is dominated by magmatic calcic amphiboles (plotting in the pargasite, edenite and magnesio-hornblende fields, $X_{Fe}$ = 0·28–0·48), up to 1 mm in size and partially overgrown by coronas of blue sodic and sodic–calcic amphiboles (Mg-riebeckite, $X_{Fe}$ = 0·38–0·46, $Na_B$ = 1·51–1·82 p.f.u., and winchite, $X_{Fe}$ = 0·27–0·46, $Na_B$ = 0·53–1·49 p.f.u., respectively) (Figs 5a and 6). Epidote, chlorite, albite (<5 %) and quartz (~5 %) are also present and accessory

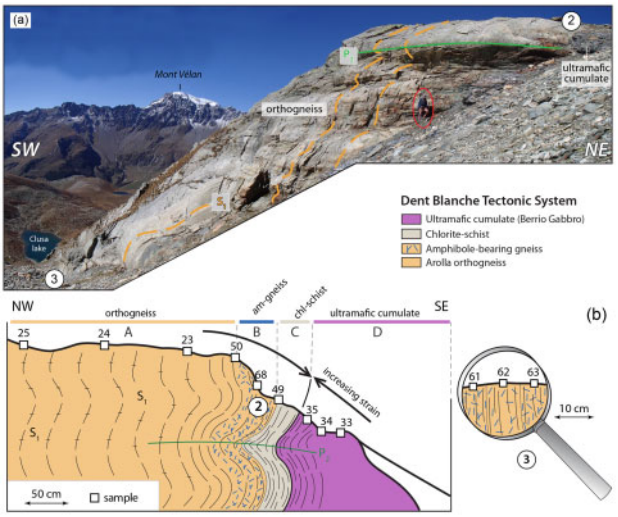



**Fig. 3.** (a) Contact between the Arolla orthogneiss and ultramafic cumulate from the Berrio Gabbro. The $S_1$ foliation in the orthogneiss and the contact between the two lithologies are affected by metre- to decametre-scale open folds. Sites 2 (45°52′25·37"N, 7°20′28·71"E) and 3 (45°52′26·78"N, 7°20′25·97"E) are indicated in the photograph. (b) Schematic cross-section of the contact between the Arolla orthogneiss and ultramafic cumulate from the Berrio gabbro. Strain increases in both lithologies towards the contact. White squares indicate sample locations and numbers refer to the sample names.

minerals (<1 %) comprise pyrite, hematite and magnetite. Fine-grained intergrowths of rutile and Ti-hematite surrounded by titanite coronas are common. Rutile and Ti-hematite are interpreted to be pseudomorphs resulting from the oxidation of original intergrowths of titanomagnetite + ilmenite, as observed in other mafic rocks (e.g. Haggert, 1991). The type-II domain is dominated by fine-grained aggregates of epidote replacing previous magmatic plagioclase and by aggregates of actinolite ($X_{Fe}$ = 0·24–0·35) and chlorite. Epidote shows significant compositional zoning, with an $Fe^{3+}/Al^{3+}$ + $Fe^{3+}$ ratio in the core of 0·09–0·20 and in the rim of 0·26–0·32 (i.e. an almost pure pistacite) (Fig. S2).

To sum up, in sample OL02, used below for the thermodynamic modelling, the observed mineral paragenesis in the type-I domain comprises sodic and sodic–calcic amphibole (magnesioriebeckite to winchite), epidote, chlorite, quartz and titanite.

### Metatonalite pods within the Berrio ultramafic rocks

Rare, medium-grained metatonalites are found as ~2 m long and ~30 cm thick layers and metre-scale pods within the massive ultramafic rocks (mainly antigorite serpentinite) of the Berrio Gabbro close to the Alpe Berrio, along and above the main path for the Col de Breuson (Fig. S1). Metatonalite pods are massive in appearance with a dense network of millimetre- to centimetre-sized patches of radiating blue and greenish amphiboles (Fig. 4a and b). Metatonalite layers locally display a weak foliation, defined by blue amphiboles

Downloaded from https://academic.oup.com/petrology/advance-article/doi/10.1093/petrology/egaa044/5810502 by guest on 29 September 2020

and layers of fine-grained fibrous aggregates of sodic pyroxene. Large crystals of quartz show undulose extinction, irregular grain boundaries and tiny fluid inclusions aligned along fracture planes. Large albite crystals locally displaying polysynthetic twinning may contain rare corroded muscovite flakes (up to 2 mm in size, Si = 3·12–3·18 p.f.u.). Quartz, albite and muscovite, as well as accessory monazite and zircon, are

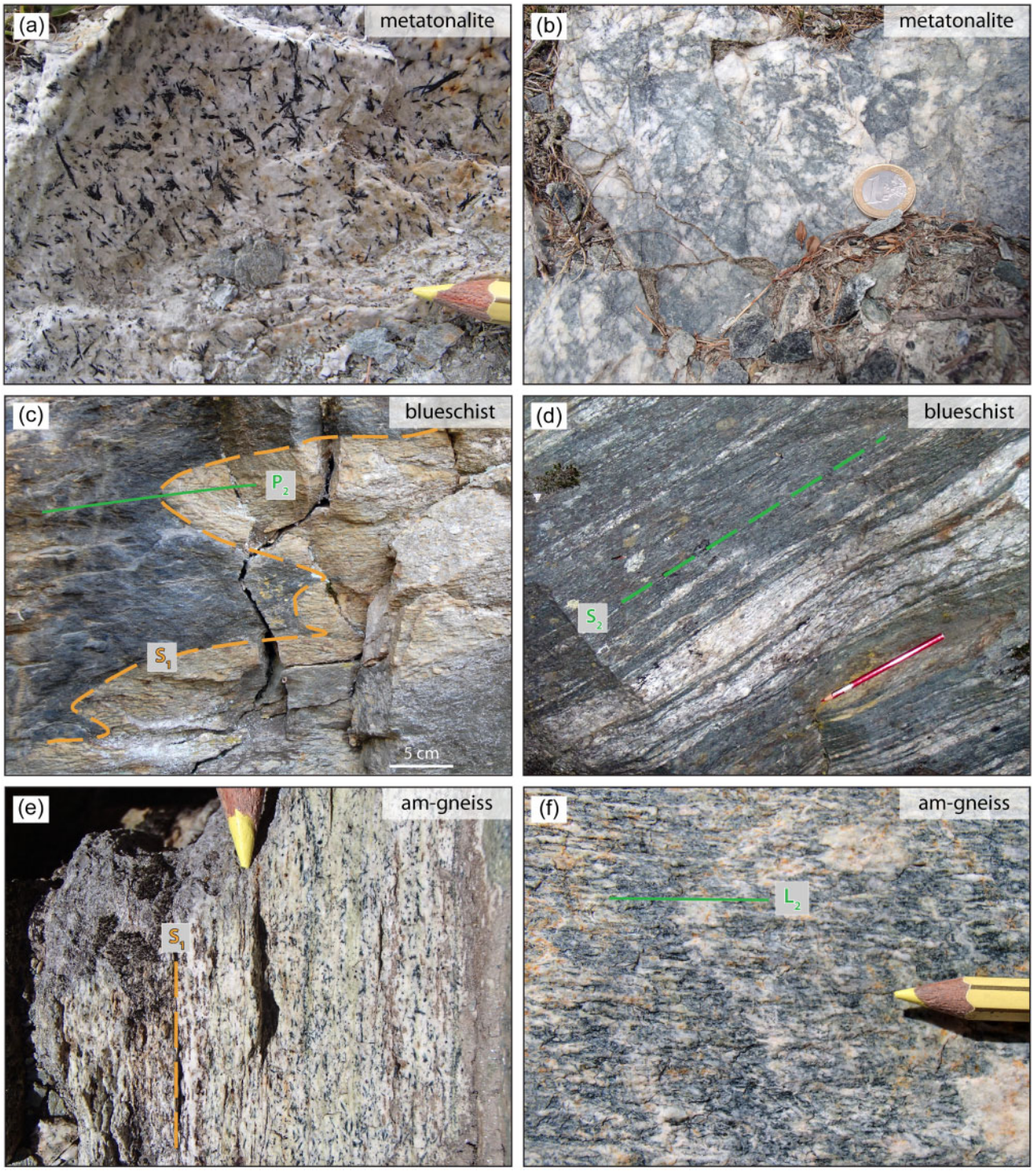



**Fig. 4.** Field aspects of the sodic amphibole-bearing rocks from the DBTS. (a) Metatonalite displaying needles of blue amphibole dispersed in an albite–quartz matrix (site 6, 45°51′43·82"N, 7°19′35·02"E). (b) Network of millimetre- to centimetre-sized patches of radiating blue and greenish amphiboles in a metatonalite pod (site 6, 45°51′43·82"N, 7°19′35·02"E). (c) Blueschist folded isoclinally together with leucocratic aplitic lenses (site 7, 45°47′13·38"N, 7°19′01·57"E). (d) In the blueschist, $S_2$ foliation is marked by epidote and quartz domains and by films of muscovite, chlorite and blue amphibole (site 7, 45°47′13·38"N, 7°19′01·57"E). (e, f) Needles of blue amphiboles in the amphibole gneiss (site 2): (e) crosscutting the mylonitic foliation $S_1$ (45°52′25·37"N, 7°20′28·71"E) and (f) the crenulation lineation $L_2$ (45°52′26·78"N, 7°20′25·97"E).

Downloaded from https://academic.oup.com/petrology/advance-article/doi/10.1093/petrology/egaa044/5810502 by guest on 29 September 2020

interpreted as relics of magmatic phases. The fine-grained recrystallized matrix consists of quartz, albite, blue amphibole, locally green clinopyroxene (Fig. 5b and c) and minor epidote, titanite and pyrite (<1%). Clinopyroxene is mainly aegirine–augite ($jd_{25}$–$aeg_{35}$–$quad_{40}$, sample OL43; Figs 5b and 7), locally with patchy zoning (from $jd_5$–$aeg_{25}$–$quad_{70}$ to $jd_{30}$–$aeg_{30}$–$quad_{40}$, sample OL44; Fig. 7b). Blue and green amphibole form

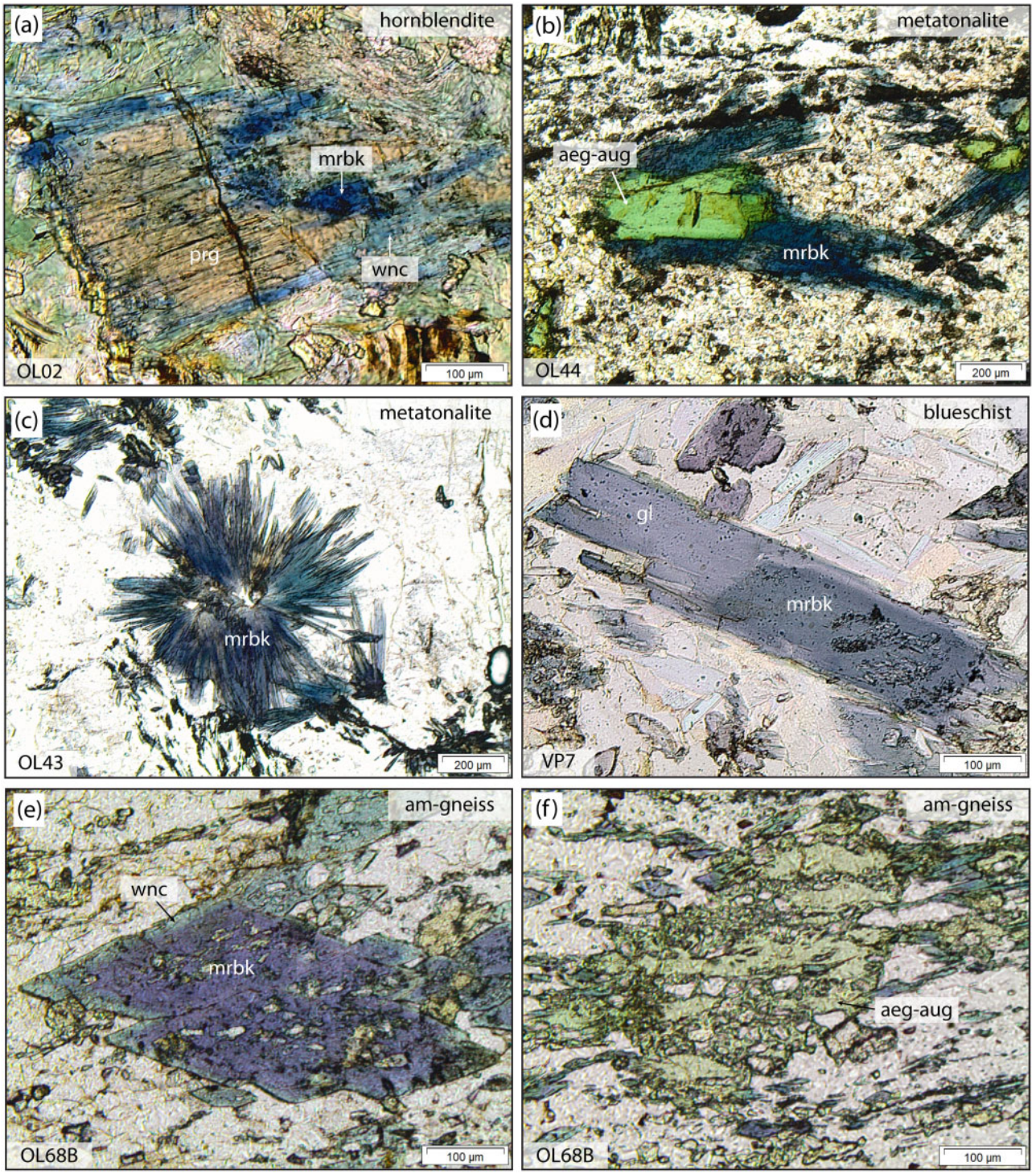



**Fig. 5.** Mineralogy and textures of the blue amphibole-bearing rocks from the DBTS. Plane-polarized light (PPL) photomicrographs. (a) Coronas of magnesioriebeckite and winchite around magmatic pargasite in the hornblendite (sample OL02, site 1). (b) Aegirine–augite surrounded by magnesioriebeckite in the metatonalite from the Berrio gabbro (sample OL44, site 6). (c) Needles of magnesioriebeckite in the albite matrix of a metatonalite from the Berrio gabbro (sample OL43, site 6). (d) A dark blue core of magnesioriebeckite surrounded by a pale blue glaucophane rim in blueschist (sample VP07, site 7). (e) Magnesioriebeckite with winchite rim in the amphibole-gneiss at the contact with ultramafic cumulate of the Berrio Gabbro (sample OL68, site 2). (f) Aegirine–augite crystals from the blue amphibole-gneiss at the contact with ultramafic cumulate of the Berrio Gabbro (site 2, sample OL68).

Downloaded from https://academic.oup.com/petrology/advance-article/doi/10.1093/petrology/egaa044/5810502 by guest on 29 September 2020

together radiating sheaves in an albite matrix. In these sheaves, blue amphibole is dominant over green amphibole. However, there is no textural argument allowing us to establish whether sodic or calcic amphiboles appear first, and thus they are considered to be stable together. Blue amphibole is slightly zoned with a darker blue core (magnesioriebeckite $X_{Fe} = 0{\cdot}15–0{\cdot}46$, $Na_B = 1{\cdot}51–1{\cdot}94$ p.f.u.) and a lighter blue rim of winchite ($X_{Fe} = 0{\cdot}20–0{\cdot}44$, $Na_B = 0{\cdot}51–1{\cdot}49$ p.f.u.) (Fig. 6). The greenish amphibole found together with magnesioriebeckite and winchite is actinolite ($X_{Fe} = 0{\cdot}24–0{\cdot}35$).

A 10–20 cm thick dark greenish grey band of chlorite-schist marks the contact between the metatonalite and the ultramafic rocks and is considered a reaction zone between the two contrasting rock types ('the blackwall'). The transition from the metatonalite to the chlorite-schist is defined by the progressive increase in the modal abundance of chlorite and the disappearance of albite (Fig. S3a). In the chlorite-schist, chlorite is zoned, with Mg content increasing from core ($X_{Mg} = 0{\cdot}77–0{\cdot}79$) to rim ($X_{Mg} = 0{\cdot}80–0{\cdot}83$). In the chlorite-schist, accessory phases include abundant zircon and rare apatite and monazite, with the latter wrapped by chlorite foliation.

To sum up, in sample OL43, used below for the thermodynamic modelling, the observed mineral paragenesis comprises quartz, albite, sodic amphibole (magnesio-riebeckite to winchite), calcic amphibole

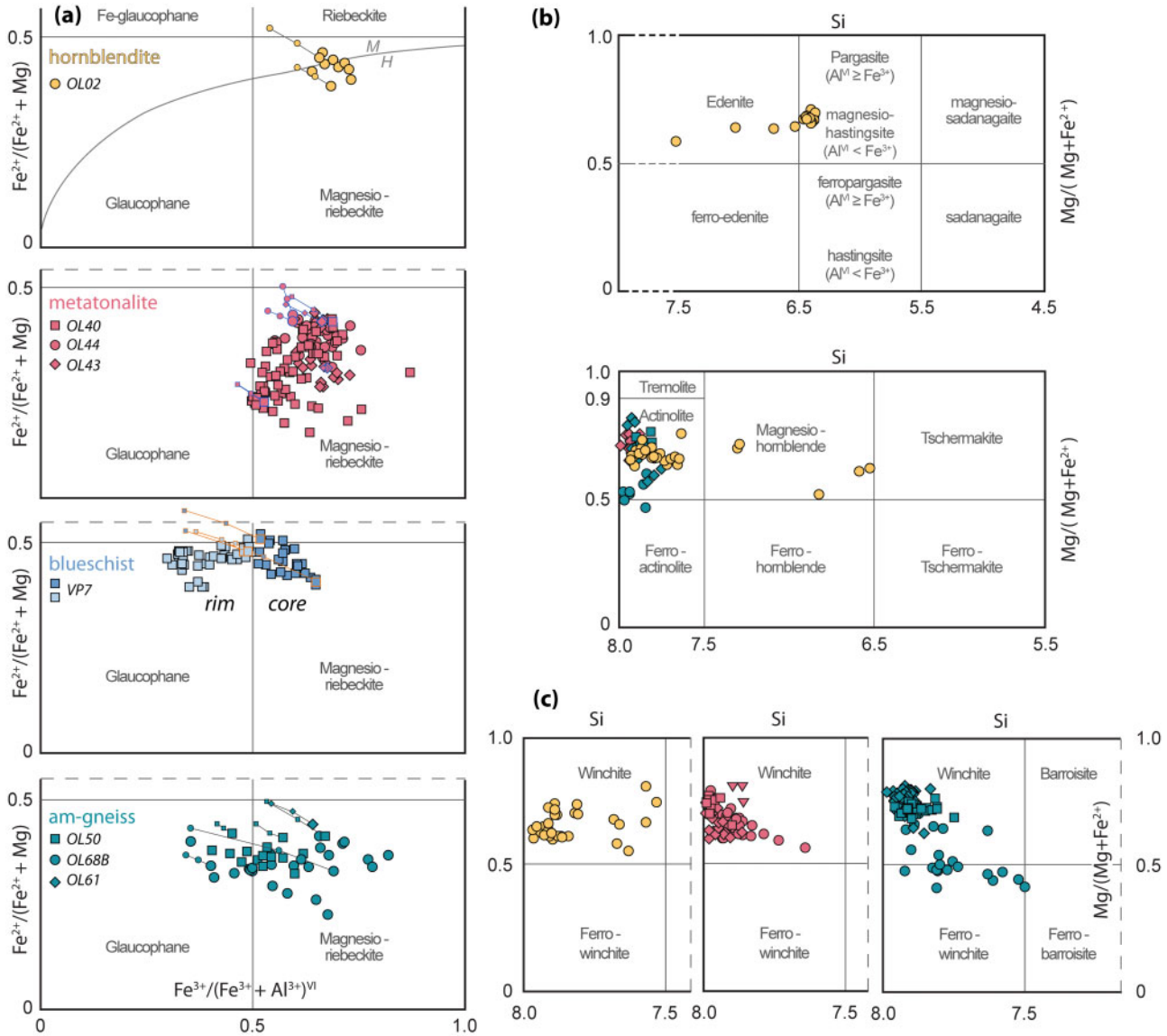



**Fig. 6.** Compositional diagrams for amphibole. (a) Na-amphibole compositions plotted in the $Fe^{3+}/(Fe^{3+} + Al^{VI})$ vs $Fe^{2+}/(Mg + Fe^{2+})$ diagram. The large symbols correspond to the recalculation giving the maximum amount of $Fe^{3+}$. The other estimations (i.e. the minimum and the mean) are plotted in the classification diagram as a fine line joining the highest estimate to the two others. The grey line marked by the letters H and M corresponds to the $fO_2$ values of hematite–magnetite buffer, as reported by Okay (1980). (b) Ca-amphibole compositions plotted in the Si (p.f.u.) vs $Mg/(Mg + Fe^{2+})$ diagram [same legend as in (a)]. (c) Na–Ca-amphibole compositions plotted in the Si (p.f.u.) vs $Mg/(Mg + Fe^{2+})$ diagram [same legend as in (a)].

Downloaded from https://academic.oup.com/petrology/advance-article/doi/10.1093/petrology/egaa044/5810502 by guest on 29 September 2020

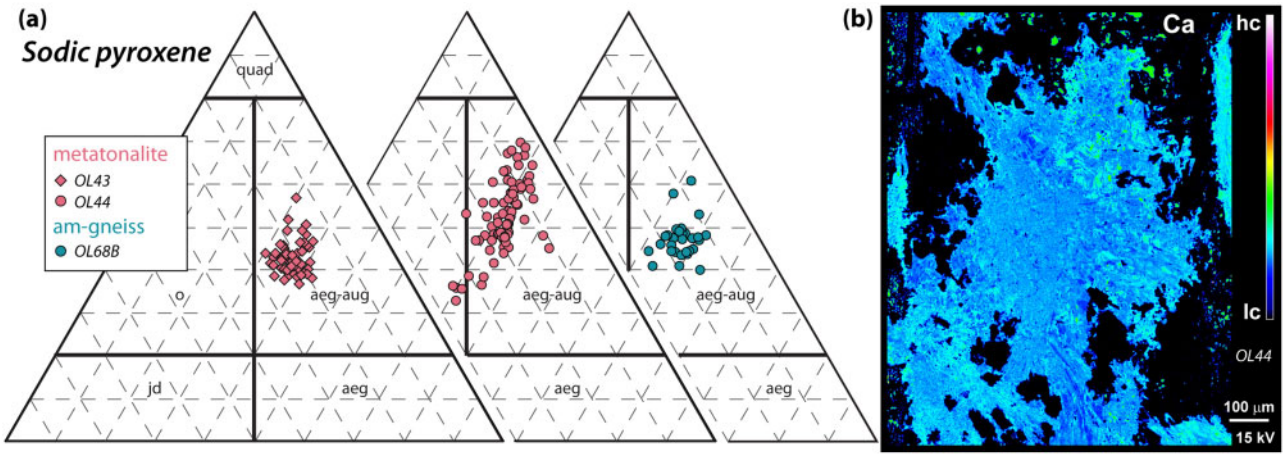



**Fig. 7.** Compositional diagrams for clinopyroxene. (a) Aegirine–augite compositions plotted in the jd–quad–aeg diagram. (b) Ca X-ray map of aegirine–augite from metatonalite (sample OL44).

(actinolite), clinopyroxene (aegirine–augite), epidote and titanite.

## Blueschist

North of Roisan village, a rather poor outcrop of dark blue fine-grained schist occurs along the path rising from Gorrey to Berrio Nemoz. The schist is isoclinally folded together with leucocratic aplitic layers (10–20 cm thick) consisting of quartz, albite and muscovite (Fig. 4c and d). The schist comprises blue amphibole, muscovite, epidote, chlorite, quartz, titanite, rare spessartine-rich garnet ($alm_{20–31}py_1gr_{21–22}spss_{47–53}andr_{0–5}$), apatite, zircon, and pyrite (<1 %). It displays a crenulation cleavage ($S_2$) with relicts of an earlier foliation ($S_1$) marked by blue amphibole and muscovite preserved in the microlithons. The new foliation ($S_2$) is defined by epidote ($Fe^{3+}/Al^{3+} + Fe^{3+}$ ranges from 0·19–25 in the core to 0·28–0·32 in the rim; Fig. S2) and quartz domains, muscovite (Si = 3·36–3·42 p.f.u.) and chlorite ($X_{Mg}$ = 0·48–0·51) films, and by blue amphibole. Muscovite contains some $Fe^{3+}$ as analyses plot above the ideal celadonite substitution (Fig. 8a). Blue amphibole (1–3 mm long) shows a dark blue core (magnesioriebeckite, $X_{Fe}$ = 0·27–0·51, $Na_B$ = 1·73–1·94 p.f.u.) and light blue rim (glaucophane, $X_{Fe}$ = 0·39–0·50, $Na_B$ = 1·87–1·98 p.f.u.) and tiny inclusions of epidote and quartz (Figs 5d and 6).

To sum up, in sample VP7, used below for the thermodynamic modelling, the observed mineral paragenesis comprises sodic amphibole (magnesioriebeckite to glaucophane), muscovite, epidote, chlorite, quartz, titanite, and garnet.

## Amphibole-gneiss at the boundary between orthogneiss and ultramafic

Sodic amphibole-bearing rocks are localized along the contact between the Arolla orthogneisses and the ultramafic rocks of the Berrio Gabbro. This contact, sharply defined at map to sample scale, is best exposed north

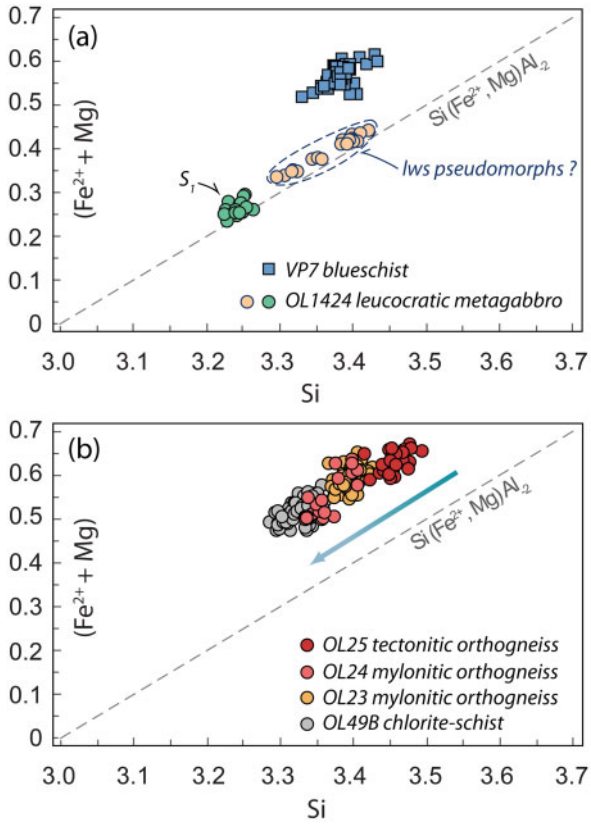



**Fig. 8.** Potassic white mica composition plotted in the Si vs $Fe^{2+}$ + Mg (p.f.u.) diagram from the leucocratic metagabbro and blueschist (a) and from samples along the profile of site 2 (b). The dashed line represents the ideal celadonitic substitution.

of the Clusa Lake (Fig. 3). There, three main lithological domains are distinguished, from the NW to the SE.

(1) The granitic orthogneisses display a strain gradient towards the contact with the ultramafic rocks (Fig. 3b): foliated orthogneisses with few magmatic feldspar and allanite porphyroclasts evolve into mylonites with a fine banded structure. Magmatic accessory

Downloaded from https://academic.oup.com/petrology/advance-article/doi/10.1093/petrology/egaa044/5810502 by guest on 29 September 2020

phases include zircon, allanite, and titanite. The mylonitic foliation $S_1$ is defined by whitish albite–quartz bands alternating with yellowish–greenish discontinuous layers of epidote ($Fe^{3+}/Al^{3+} + Fe^{3+} = 0{\cdot}16$–$0{\cdot}23$ in the core and 0·26–0·32 in the rim; Fig. S2), chlorite and muscovite (Si = 3·42–3·50 p.f.u., 3·34–3·41 p.f.u., 3·35–3·45 p.f.u. in OL25, OL24 and OL23 respectively). Analyses of muscovite plot above the line of ideal celadonite substitution, indicating the presence of $Fe^{3+}$ (Fig. 8b).

(2) A reaction zone, about 0·5 m thick, is observed along the contact between the Arolla orthogneisses (A in Fig. 3b) and the Berrio ultramafic rocks (D in Fig. 3b). The reaction zone (B and C in Fig. 3b) displays two types of lithologies.

The first one is an ~10–20 cm thick zone of amphibole-gneiss, yellowish–greenish in colour, sometimes showing a centimetre-scale layering. It is characterized by small needles of blue amphibole and rare pale green clinopyroxene, both displaying numerous quartz inclusions (B in Fig. 3b). Only locally are the blue amphibole needles aligned parallel to the stretching lineation $L_1$. In most cases, blue amphibole defines rosettes or sheaves (up to 3 mm in size), which are dispersed in a quartz–albite-rich matrix, generally without a shape-preferred orientation (Fig. 4e). Growth of these rosettes may be contemporaneous with, or later than, the crenulation lineation $L_2$ (Fig. 4f). Blue amphiboles are slightly zoned, with darker blue cores and lighter blue or greenish rims, whatever their structural position (Fig. 5e). Cores are magnesioriebeckite and rarely glaucophane ($X_{Fe} = 0{\cdot}22$–$0{\cdot}41$ and 0·31–0·40, respectively; $Na_B$ = 1·56–1·91 and 1·90–1·92 p.f.u. respectively), whereas rims are winchite and rarely actinolite ($X_{Fe}$ = 0·18–0·51 and 0·40–0·54, respectively) (Fig. 6). Pale green clinopyroxene (Fig. 5f) is aegirine–augite ($jd_{25}$–$aeg_{35}$–$quad_{40}$, sample OL68) (Fig. 7). Epidote shows significant compositional zoning, with an $Fe^{3+}/Al^{3+} + Fe^{3+}$ ratio of 0·15–0·23 in the core and of 0·25–0·32 in the rim (Fig. S2). A few titanite crystals containing tiny rutile grains are dispersed in the rock, together with idioblastic crystals of hematite, magnetite and pyrite (<1 %).

Second, an ~10 cm thick layer of dark greenish grey fine-grained chlorite-schist (C in Fig. 3b) is found against the ultramafic rocks. At the interface between the amphibole-gneiss and the chlorite-schist, an ~3 mm thick layer of randomly oriented muscovite flakes (Si = 3·30–3·39 p.f.u.) is observed (Fig. S3b). Muscovite contains some $Fe^{3+}$ because analyses plot above the line of ideal celadonite substitution (Fig. 8b). The chlorite-schist is essentially made of zoned chlorite, with Mg content increasing from core ($X_{Mg}$ = 0·67–0·79) to rim ($X_{Mg}$ = 0·82–0·86) (Fig. S3b). The foliation is defined by the shape fabric of chlorite and by aligned epidote crystals ($X_{Ps}$ = 0·25–0·29; Fig. S2). The former presence of porphyroclasts is recorded by the presence of chlorite aggregates [after plagioclase(?), e.g. Müntener *et al.*, 2010] wrapped by the foliation. In the chlorite-schist, accessory phases include numerous zircon grains, apatite and a few allanite crystals.

(3) The Berrio ultramafic rocks (wehrlite; see Manzotti *et al.*, 2017, for details) also display a strain gradient towards the contact with the orthogneiss. Unfoliated rocks that preserve their primary magmatic texture progressively evolve to mylonitic serpentinites (a few centimetres thick; Fig. 3b). In the undeformed domain, the rock comprises a serpentine mesh with magnetite (interpreted as pseudomorphs after olivine), and Cr-magnetite and Mg-chlorite (interpreted to replace Cr-spinel). Fine-grained aggregates of tremolite–calcite–Mg-chlorite–titanite are interpreted to pseudomorph clinopyroxene. The intercumulus phases are completely recrystallized into actinolite–tremolite. In the mylonitic serpentinites, a pervasive foliation, oriented parallel to the contact with the orthogneisses, is defined by an alternation of serpentine, chlorite, and magnetite layers. Talc occurs as veins crosscutting or parallel to the main foliation. The modal proportion of talc increases towards the contact.

To sum up, in sample OL68B, used below for the thermodynamic modelling, the observed mineral paragenesis comprises quartz, albite, epidote, sodic amphibole (magnesioriebeckite to winchite), clinopyroxene (aegirine–augite), and titanite.

## Leucocratic metagabbro

Leucocratic metagabbro occurs as decametre-thick layers in the Berrio Gabbro and is always mylonitic. Examples can be observed in the Col Cornet–Monte Berrio area, in the western portion of the mafic complex, along the contact with the Arolla orthogneiss (Fig. S1). The inferred original assemblage plagioclase + clinopyroxene + minor spinel is replaced by Alpine metamorphic minerals. The rocks show a pervasive Alpine mylonitic foliation $S_1$, marked by tiny crystals of muscovite (Si = 3·22–3·26 p.f.u.), and Mg-chlorite ($X_{Mg}$ = 0·76–0·90) (replacing magmatic clinopyroxene), alternating with zoisite layers (replacing magmatic plagioclase). The few rectangular-shaped aggregates consisting of muscovite (Si = 3·30–3·42 p.f.u.) and fine-grained clinozoisite and Mg-chlorite may represent pseudomorphs after former lawsonite. The fit of the composition of muscovite with the theoretical line of the $Si(Fe,Mg)Al_{-2}$ substitution suggests that the $Fe^{3+}$ content is negligible (Fig. 8a). Locally, clinozoisite layers wrap around plagioclase porphyroclasts (now consisting of pure albite). Green slightly elongated patches up to 2 mm in size are scattered in the leucocratic gabbro. In thin section they consist of Cr-rich muscovite ('fuchsite'; Cr content up to 6·6 wt%) and chromian pumpellyite (Cr content up to 16·40 wt%) and are interpreted to replace Cr-rich spinel. Sodic amphibole has never been observed in the leucocratic metagabbro.

To sum up, in sample OL1424, used below for the thermodynamic modelling, the Cr-bearing phases (i.e. fuchsite and pumpellyite) are absent and the observed

Downloaded from https://academic.oup.com/petrology/advance-article/doi/10.1093/petrology/egaa044/5810502 by guest on 29 September 2020

synfolial mineral assemblage is epidote, chlorite, muscovite, albite, and quartz.

A summary of the relationships between deformation and growth in the studied samples (Table 3) shows that the sodic amphiboles grew at peak *P*–*T* conditions and eventually recrystallized after the mylonitic deformation in the amphibole-gneiss.

## WHOLE-ROCK GEOCHEMISTRY

### Hornblendite lenses in the Berrio Gabbro

Hornblendites (samples OL02, OL03 and OL04) are ultramafic rocks ($SiO_2$ 36·41–42·08 wt%), rich in $Fe_2O_3$* (13·01–21·92 wt%) and low in alkalis (0·39–2·61 wt%) (Fig. 9a). They display elevated $Fe^{3+}$/Fe* ratios (0·29–0·37; Table 4). Calculated Mg# values fall within the range 61–67 (Fig. 9c). Their rare earth element (REE) patterns are relatively flat ($1{\cdot}79 < La_N/Yb_N < 2{\cdot}83$; $2{\cdot}37 < Sm_N/Yb_N < 2{\cdot}80$).

### Metatonalite pods within the Berrio ultramafic rocks

The metatonalites are silica-rich ($SiO_2$ 68·79–72·61 wt%), poor in $Fe_2O_3$* (1·61–2·45 wt%) and rich in $Na_2O$ (8·76–9·71 wt%) (Fig. 9a and c). Their $K_2O$ content is negligible (<0·1 wt%). The $Fe^{3+}$/Fe* ratio varies from 0·27 to 0·40 (Table 4). They display a light REE (LREE)-enriched pattern ($La_N/Yb_N$ up to 85·21). Three samples display negative Eu anomalies (Eu/Eu* = 0·17–0·72) and one sample shows a positive Eu anomaly (Eu/Eu* = 1·64) (Fig. 9e). The chlorite-schist at the contact with the ultramafic rocks displays a strong decrease in $SiO_2$ (29·23 wt%) and an important increase in $Al_2O_3$ (18·66 wt%), $Fe_2O_3$* (13·59 wt%) and MgO (25·95 wt%). The loss on ignition (LOI) strongly increases towards the reaction zone (from 0·77 wt% in the metatonalite to 11·13 wt% in the chlorite-schist) and may be attributed to the presence of $H_2O$ structurally bound principally in chlorite. Metatonalite and chlorite-schist display similar REE patterns (Fig. 9e), suggesting that both lithologies evolved from the same protolith.

### Blueschist

The blueschist displays an intermediate $SiO_2$ content (57·92 wt%) and a relatively high alkali content (6·41 wt%) (Fig. 9b). It is rich in $Fe_2O_3$* (9·09 wt%), with a relatively high $Fe^{3+}$/Fe* ratio (0·49; Table 4). Assuming that the protolith of the blueschist was a volcanic rock, its composition plots in the trachyandesite field in both the total alkalis–silica (TAS) (Le Maître, 2002) and Zr/Ti versus $SiO_2$ diagrams (Winchester & Floyd, 1977).

### Reaction zone at the boundary between orthogneiss and ultramafic rock

A geochemical profile comprising 12 samples was traced across the reaction zone between the Arolla orthogneisses and the Berrio ultramafic rocks (site 2), by far the best outcrop of this reaction zone (Fig. 3a and b). The profile comprises three samples of orthogneisses, six samples of amphibole-gneisses and three samples of ultramafic rocks (Figs 3b and 10).

The Arolla orthogneisses (samples OL25, OL24 and OL23) show an acidic composition ($SiO_2$ = 61·75–71·19 wt%) and high alkali content (7·18–7·79 wt%). The $Na_2O/K_2O$ ratio drastically increases from the orthogneiss to the amphibole-gneiss. The amphibole-gneisses display variable $SiO_2$ content (55·89–72·42 wt%). They are rich in $Na_2O$ (5·62–10·74 wt%) but very low in $K_2O$ (<1 wt%) (Fig. 9b and d). They show a large variation in $Fe_2O_3$* (0·57–6·13 wt%) content and high $Fe^{3+}$/Fe* ratios (0·43–0·50).

Some trends in major and trace elements are evident along the profile (Fig. 10, Table S11). In the orthogneisses, MgO and $Al_2O_3$ contents increase towards the contact with the ultramafic rocks, whereas $SiO_2$ decreases (from A to C in Fig. 10b). CaO and $Na_2O$ contents display a continuous increase (from A to B) followed by a rapid decrease close to the contact (C; Table S11). The LOI increases abruptly from 1·20 wt% in the orthogneiss (A) to 11·26 wt% in the chlorite-schist (C). Its concentration correlates with the modal abundance of chlorite (~90 %) in the schist and is thus attributed to the presence of structurally bound $H_2O$. The molar $Fe^{3+}$/Fe* ratio decreases from 0·50 to 0·40 (A) followed by an increase up to 0·67 (B) and decrease down to 0·05 (C, chlorite-schist). Some of the large ion lithophile elements (LILE; e.g. K, Ba, Rb and Cs, Table S13) decrease in concentration towards the contact with the ultramafic rocks (A to B). This could be related to the absence of muscovite in the amphibole-gneiss. This trend is followed by a rapid and localized increase in LILE corresponding to a thin layer of muscovite (sample 49B, C; Fig. 10a) and then by an abrupt disappearance of these

**Table 3:** A summary of the deformation–growth relationships in the studied rocks

| Lithology | Deformation | Texture | Zoning | Timing of growth |
|---|---|---|---|---|
| Hornblendite | Undeformed | Coronitic overgrowth on magmatic amphibole | Unzoned | Peak |
| Metatonalite | Undeformed | Needles and rosettes and coronas around sodic clinopyroxene | Unzoned | Prograde to peak |
| Blueschist | Foliation $S_1$ + crenulation $S_2$ | Aligned along the $S_1$ foliation and passively reoriented along the crenulation planes $S_2$ | Zoned (mrbk core, gl rim) | Prograde to peak |
| Amphibole-gneiss | Mylonitic foliation $S_1$ | Parallel to the $S_1$ and randomly oriented cross-cutting the $S_1$ | Zoned (mrbk at the core, wnc rim) | Peak to post |

Downloaded from https://academic.oup.com/petrology/advance-article/doi/10.1093/petrology/egaa044/5810502 by guest on 29 September 2020

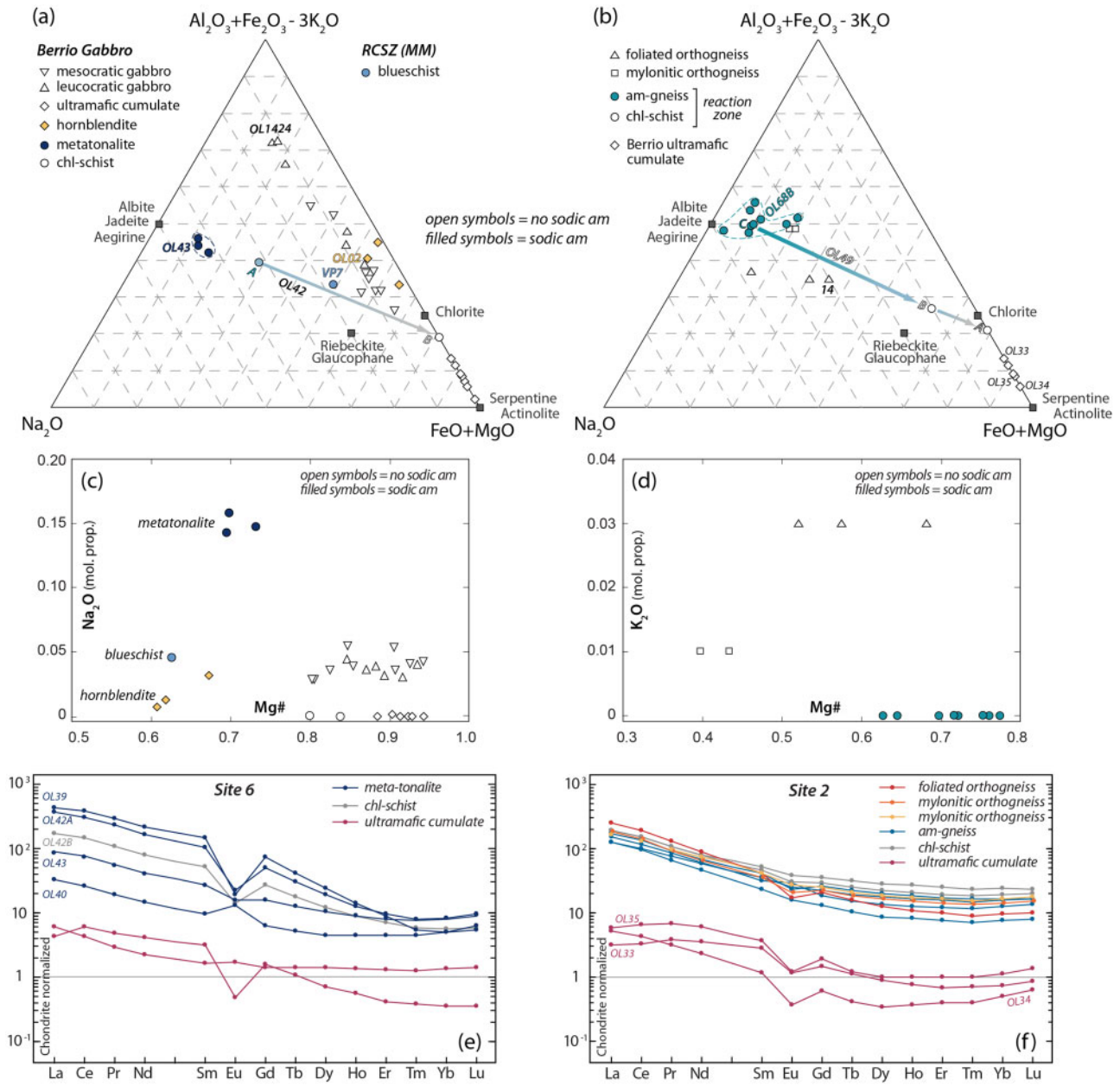



**Fig. 9.** Whole-rock composition of the studied samples. (a) Ternary diagram showing the bulk-rock compositions of the Berrio Gabbro rock types (sites 1 and 6) and blueschist (site 7). The analyses of leucocratic and mesocratic gabbros are from Manzotti *et al.* (2017). (b) Ternary diagram showing the bulk-rock compositions of orthogneiss, am-gneiss and ultramafic cumulate from sites 2, 3, 4, and 5. Strictly speaking, the ternary diagrams are projections from quartz, muscovite, clinozoisite/epidote and vapour. It should be noted, however, that some of these phases are not present in all lithologies (especially quartz and epidote in the chlorite-schist and in the ultramafic cumulate). (c) Mg# vs $Na_2O$ (expressed as molecular proportions) diagram for the Berrio Gabbro lithologies and blueschist. Open symbols refer to rocks that do not contain sodic amphibole; filled symbols refer to rocks containing sodic amphibole (i.e. metatonalite, hornblendite, and blueschist). Metatonalite displays low Mg# and high $Na_2O$ content. Hornblendite and blueschist show low Mg# and moderate $Na_2O$ content. (d) Mg# vs $K_2O$ (expressed in molecular proportions) diagram for the orthogneiss and amphibole-gneiss. Open symbols refer to rocks that do not contain sodic amphibole; filled symbols refer to rocks containing sodic amphibole. Amphibole-gneisses display very low $K_2O$ content. (e) Trace element compositions of the samples from site 6. The similarity between the pattern of the metatonalite and chlorite-schist, indicating that both evolve from the same protolith, should be noted. (f) Trace element compositions of the samples from site 2. The similarity in the pattern of the orthogneisses and chlorite-schist, indicating that they all evolve from the same protolith, should be noted. Chondrite values are from Sun & McDonough (1989).

elements approaching the contact with the ultramafic rock (sample 49A, C). In the ultramafic rocks, the $Fe^{3+}$/Fe* ratio decreases from 0·36 to 0·20 towards the contact with the orthogneisses.

Along the profile, the orthogneiss, the amphibole-gneiss and the chlorite-schist display similar LREE-enriched patterns (Fig. 9f), indicating that the three lithological units were derived from the same granitic

Downloaded from https://academic.oup.com/petrology/advance-article/doi/10.1093/petrology/egaa044/5810502 by guest on 29 September 2020

**Table 4:** Synthesis of the main chemical characters of the studied rocks

| | Metamorphic rock | | | | | | Metasomatic rock | |
|---|---|---|---|---|---|---|---|---|
| | Ultramafic cumulate | Mesocratic gabbro | Horn-blendite* | Meta-tonalite* | Leucocratic gabbro | Orthogneiss | Roisan blueschist* | Am-gneiss* | Chlorite-schist |
| $Fe_2O_3$* (wt%) | 6·19–16·29 | 3·37–8·59 | 13·01–21·92 | 1·61–3·26 | 0·97–4·37 | 2·72–5·11 | 9·09 | 0·57–6·13 | 10·92–13·59 |
| FeO* (wt%) | 5·57–14·66 | 3·03–7·73 | 11·71–19·72 | 1·45–2·93 | 0·87–3·93 | 2·45–4·60 | 8·18 | 0·51–5·52 | 9·83–12·23 |
| FeO* + MgO (wt%) | 36·68–46·28 | 9·66–17·11 | 19·19–28·74 | 2·52–3·77 | 2·86–15·00 | 3·41–6·28 | 10·79 | 0·74–7·84 | 36·68–38·17 |
| Mg# | 88–94 | 66–82 | 61–67 | 69–75 | 85 | 52–68 | 63 | 71–77 | 80–84 |
| $Fe^{2+}/Fe^{2+}$ + Mg | 0·06–0·12 | 0·06–0·20 | 0·33–0·39 | 0·27–0·31 | 0·07–0·15 | 0·23–0·43 | 0·37 | 0·23–0·37 | 0·16–0·20 |
| $Fe^{3+}/Fe^{3+} + Fe^{2+}$ | 0·15–0·40 | 0·18–0·66 | 0·29–0·37 | 0·27–0·40 | 0·18–0·60 | 0·27–0·61 | 0·49 | 0·35–0·67 | 0·03–0·05 |
| Na/Na + Ca | 0·00–0·01 | 0·11–0·22 | 0·02–0·13 | 0·90–0·94 | 0·11–0·18 | 0·67–0·96 | 0·39 | 0·50–0·94 | 0·00–0·03 |

*Rock types containing sodic amphibole and/or sodic pyroxene.

protolith. Considering the entire profile, the most prominent feature is the decrease of all the high field strength elements (HFSE) and LILE at the transition from the granitic orthogneiss to the ultramafic rocks.

## THERMODYNAMIC MODELLING

Thermodynamic modelling was used to constrain the *P–T–X* ($Fe_2O_3$ and $H_2O$) conditions at which sodic amphibole ('gl') and/or sodic pyroxene ('cpx') developed in different rock types from the DBTS (i.e. hornblendite OL02, metatonalite OL43, blueschist VP7, and am-gneiss OL68B). For comparison, a leucocratic metagabbro (OL1424) and an orthogneiss (14), both devoid of sodic amphibole and sodic pyroxene, were modelled.

### *P–T* modelling

#### *Hornblendite OL02*

In the hornblendite (OL02), blue amphibole only occurs as overgrowths on magmatic pargasite in the type-I domains (see the section 'Petrography and mineral chemistry'). To calculate phase diagrams considering only metamorphic minerals, the chemical contribution of magmatic pargasite (20 %, estimated by point counting) was subtracted from the bulk chemical composition obtained by X-ray fluorescence (XRF). The corrected bulk chemistry is considered to be a better approximation of the effective bulk composition during metamorphic recrystallization and was used to calculate a *P–T* pseudosection (Fig. 11a) in the system MnNCFMASHTO. In this model, the transition from 'greenschist-facies' to 'blueschist-facies' assemblages occurs over a narrow *P* interval (from 7·5 to 8·5 kbar depending on *T*; Fig. 11a). In this limited *P* range (less than 1 kbar), the $Na_2O$ component is transferred from ab to gl. Correspondingly, the amphibole mode isopleths show that its modal abundance rapidly increases from 5 to 20 vol%. The modal abundance of sodic amphibole modelled in the field gl–ep–pa–chl–q–sph, which corresponds to the observed assemblage in thin section, is 15–20 vol%. The modelled composition of the sodic amphibole ('gl') plots in the glaucophane field, close to the boundary of Fe-glaucophane (Fig. 12a), and does not change significantly with *P*. The observed chemistry of sodic amphibole in the studied sample plots in the magnesio-riebeckite field: it has the same $Fe^{2+}$ content as predicted by the numerical modelling and a slightly higher $Fe^{3+}$ content than predicted. Paragonite is predicted to be stable above 4 kbar at 350 °C and 9 kbar at 480 °C, but has never been observed. However, its modal amount is small. For example, in the field gl–ep–pa–chl–sph–q–ab, paragonite modal amount increases from 1 to 5 vol% with increasing *P* (Fig. 11a).

Downloaded from https://academic.oup.com/petrology/advance-article/doi/10.1093/petrology/egaa044/5810502 by guest on 29 September 2020

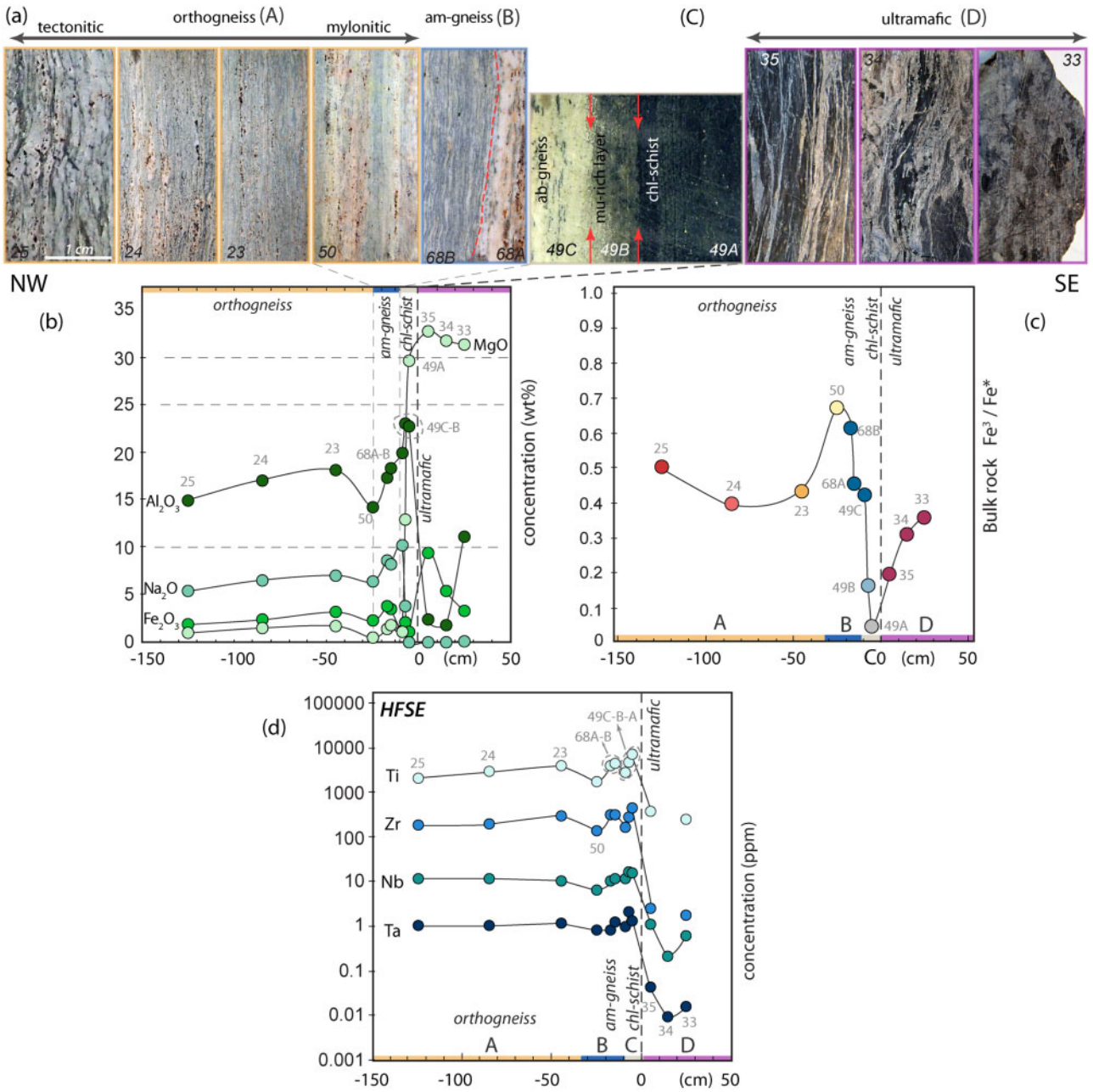



**Fig. 10.** (a) Sample photographs along the profile traced at the contact between the Arolla granitic orthogneiss and the ultramafic cumulates of the Berrio Gabbro (site 2, Fig. 3). (b–e) Chemical composition along the studied profile: (b, c) major elements; (d) trace elements (HFSE). For clarity, only the samples' number is reported in the figure. The colours at the bottom of the diagrams refer to the different lithologies along the section, as in Fig. 3b.

### *Metatonalite OL43*

A *P–T* pseudosection (Fig. 11b) has been calculated in the MnNCKFMASHTO model system for the bulk composition obtained by XRF. Three amphiboles are present in the calculated phase diagram. A sodic amphibole is stable at rather high *P*. At low *P*, actinolite is stable at low *T*, and hornblende becomes stable at *T* higher than *c.* 450 °C. Owing to the continuous nature of the reactions, fields with two or three coexisting amphiboles (act + gl, act + hb, gl + hb, act + gl + hb) are present in the phase diagram. The transition from greenschist-facies assemblages (i.e. actinolite-bearing) to blueschist-facies assemblages (i.e. glaucophane-bearing) occupies a large *P–T* band, up to 2 kbar wide at a given *T*. Sodic amphibole is stable down to 5 kbar at 350 °C and 7 kbar at 470 °C. With increasing *P* (at a fixed T of *c.* 400 °C), the modal proportion of sodic amphibole significantly increases (from 2 to 6 vol%) once actinolite is consumed and epidote appears.

The mineral assemblage gl–act–cpx–ep–sph–q–ab, observed in thin section, is stable in the range 8–9 kbar and 430–480 °C. The chemical composition of both the

Downloaded from https://academic.oup.com/petrology/advance-article/doi/10.1093/petrology/egaa044/5810502 by guest on 29 September 2020

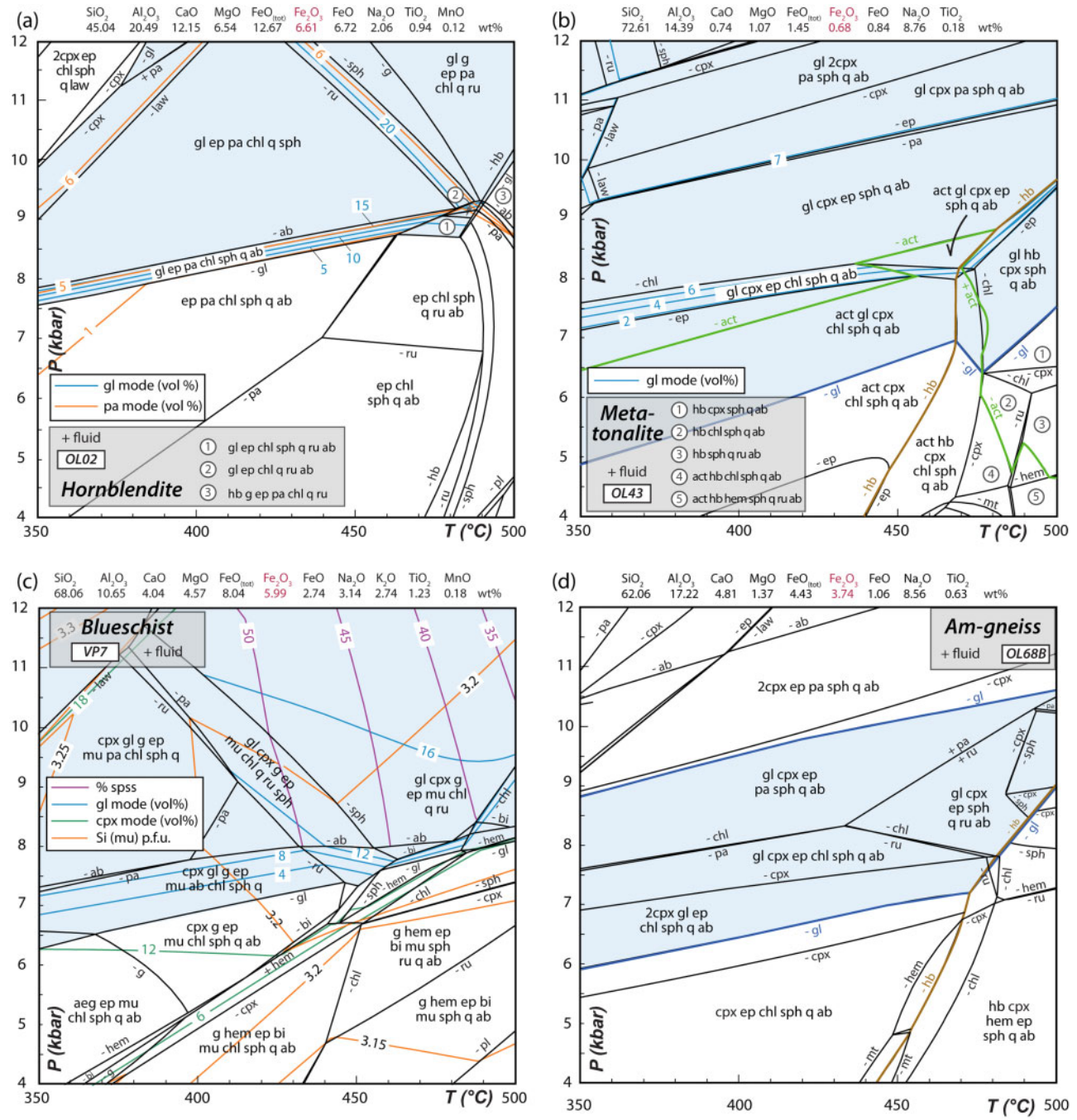



**Fig. 11.** *P–T* pseudosections for the studied samples: (a) OL02, hornblendite; (b) OL43, metatonalite; (c) blueschist VP7; (d) am-gneiss OL68B. The blue field indicates the *P–T* space where sodic amphibole ('gl') is stable. Blue lines in (a) and (b) show the glaucophane modal amount (vol%). Muscovite compositional isopleths for Si (in p.f.u.) are reported in orange in (c). The amount of $Fe_2O_3$ used for the *P–T* calculation is highlighted in red. The grey arrows indicate two possible *P–T* path consistent with mineral assemblages. For clarity, some fields are not labelled; their mineral assemblages can be deduced from assemblages in adjacent fields.

sodic amphibole and the sodic pyroxene displays a decreasing $Fe^{3+}/(Fe^{3+} + Al^{3+})$ ratio with increasing *P* (Fig. 12a, c and d). The measured compositions of sodic amphibole and sodic pyroxene in this sample suggest a *P* of ~7 kbar and 7–9 kbar respectively (Figs 6 and 7).

### *Blueschist VP7*

A *P–T* pseudosection (Fig. 11c) has been calculated in the MnNCKFMASHTO model system for the bulk composition obtained by XRF. Sodic amphibole ('gl') is predicted to be stable at *P* higher than ~6–8 kbar in the *T*

Downloaded from https://academic.oup.com/petrology/advance-article/doi/10.1093/petrology/egaa044/5810502 by guest on 29 September 2020

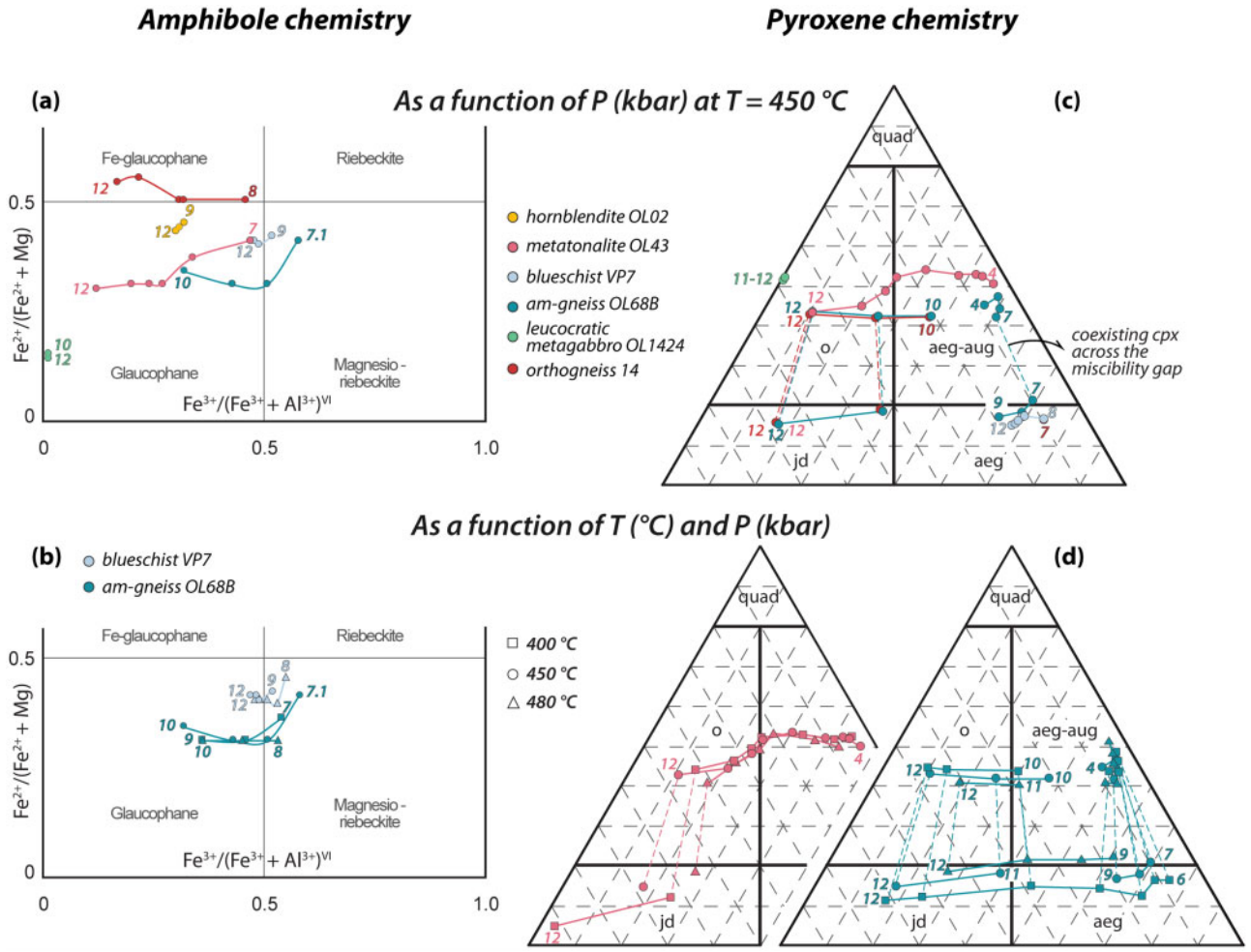



**Fig. 12.** Mineral chemistry of amphibole and clinopyroxene as predicted by thermodynamic modelling, from 4 to 12 kbar at 450 °C (a) and across the *P*–*T* space (b) (4–12 kbar at 400, 450 and 480 °C). Numbers are pressures in kbar. Dashed lines show coexisting minerals.

range considered (350–500 °C), always with a sodic pyroxene. The assemblage gl–cpx–g–ep–mu–chl–q–sph, which best approximates the observations, is stable in the triangular field at ~7·5–9 kbar and ~400–430 °C (Fig. 11c). Calculated isopleths suggest that 6–12 vol% pyroxene is present in this field.

The composition of the modelled sodic amphibole plots close to the boundary between the magnesioriebeckite and glaucophane (Fig. 12a and b), similar to the results of the electron microprobe (Fig. 6a). The measured compositional variations may be interpreted as recording a slight increase in *P* during amphibole growth (Fig. 6a). The composition of the modelled sodic pyroxene plots in the field of aegirine (Fig. 12c). However, sodic pyroxene has not been observed in the studied sample. The modelled garnet compositional isopleths for $X_{spss}$ constrain the growth of garnet to about 400–450 °C (Fig. 11c).

### *Amphibole-gneiss OL68B*

A *P*–*T* pseudosection (Fig. 11d) has been calculated in the NCFMASHTO model system for the bulk composition obtained by XRF. The calculated phase diagram displays a large *P* stability field for sodic amphibole at intermediate *P* range and a hornblende stability field above 450 °C. Above 9–10 kbar, sodic amphibole disappears and is replaced by assemblages with two cpx, namely omphacite and jadeite (Fig. 12c and d). The sodic pyroxenes display a complex behaviour with increasing *P*. Considering an isothermal section at 450 °C, a sodic pyroxene with an aegirine–augite composition is stable at *P* lower than 6 kbar (Fig. 12c). At slightly higher *P* (6–8 kbar), two pyroxenes become stable, with a composition of aegirine–augite and aegirine. With increasing *P* (8–10 kbar), only one sodic pyroxene is stable, with a composition first of an aegirine then of an aegirine–augite. Above 10 kbar, two pyroxenes are stable again, with an omphacite and jadeite composition. Paragonite is stable at $P > 7{\cdot}5$–10 kbar. Chlorite disappears at $P < 7{\cdot}5$–8 kbar at *T* higher than 450 °C.

The observed mineral assemblage gl–cpx–ep–sph–q–ab is partially reproduced in the calculated phase diagram with one additional phase (either paragonite or

Downloaded from https://academic.oup.com/petrology/advance-article/doi/10.1093/petrology/egaa044/5810502 by guest on 29 September 2020

chlorite or rutile). In each case, their modelled modal abundance is less than ~1 vol%. The composition of the sodic pyroxene measured in the studied sample is similar to the one predicted by the numerical model at 10–11 kbar (Fig. 7). The composition of the calculated sodic amphibole displays decreasing $Fe^{3+}/(Fe^{3+} + Al^{3+})$ with increasing *P* (Fig. 12a and b). At 7–9 kbar, its composition is similar to the one measured in the studied sample (Fig. 6a).

### *Leucocratic metagabbro OL1424*

Amongst the samples of the leucocratic metagabbro, OL1424 was chosen because it lacks Cr-bearing phases, and therefore Cr could be neglected in the numerical modelling. A *P*–*T* pseudosection (Fig. 13a) has been calculated in the NCKFMASHO model system for the bulk composition obtained by XRF. In this pseudosection, sodic amphibole (with a glaucophane composition; Fig. 12a) is predicted to be stable above 9 kbar at 370 °C and ~11 kbar at 500 °C, paragonite from 7 kbar at 350 °C and 9 kbar at 500 °C, whereas sodic pyroxene (with an omphacite composition; Fig. 12c) appears at 8·5 kbar and 350 °C and 10·5 kbar and 500 °C. Lawsonite is stable above 7·2 kbar at 350 °C and 12 kbar at 425 °C. This collectively indicates that the glaucophane-bearing, blueschist-facies parageneses are stable at high *P* (> 9 kbar), whereas the greenschist-facies parageneses (i.e. ep–mu–chl–q–ab and act–ep–mu–chl–q–ab) occupy a large *T* range below ~9 kbar.

The observed mineral assemblage ep–mu–chl–ab–q is predicted to be stable in the range 350–400 °C and 4·5–9 kbar. The composition of syn-$S_1$ muscovite (Si = 3·22–3·26 p.f.u.) suggests equilibration in a *P*–*T* band between 360–390 °C at 4 kbar and 440–470 °C at ~10 kbar in the neighbouring, actinolite-bearing field. Indeed, if actinolite was also present, the assemblage would be stable in a larger field ranging from 350–400 °C at 4 kbar to 430–500 °C at 9·5 kbar (dashed lines in Fig. 13a). Calculated actinolite mode is lower than 1·2 vol% in this field, potentially explaining why this mineral was not found. Si-rich muscovite (Si > 3·30 p.f.u.), found in possible pseudomorphs after lawsonite, is predicted to be stable at low *P*–*T* conditions (*P* < 8·5 kbar, *T* < 370 °C).

### *Orthogneiss 14*

A *P*–*T* pseudosection (Fig. 13b) has been calculated in the NCKFMASHTO model system for the bulk composition of an orthogneiss reported by Diehl *et al.* (1952). The rock consists of muscovite, quartz, albite, epidote, chlorite, and titanite, but systematically lacks sodic amphibole. In the pseudosection, this assemblage is predicted in the LT–LP corner, at *T* < 400 °C and *P* < 6 kbar. Sodic amphibole is predicted in a wide range of *P*–*T* conditions (at *P* higher than ~6 kbar). Its composition plots in the Fe-glaucophane field close to the limit with the glaucophane field (Fig. 12a) and displays an $Fe^{3+}$ content decreasing with increasing *P*. The mineral assemblage gl–ep–mu–chl–sph–q–ab is modelled in the *T* interval 350–460 °C between ~6 and 8·5 kbar

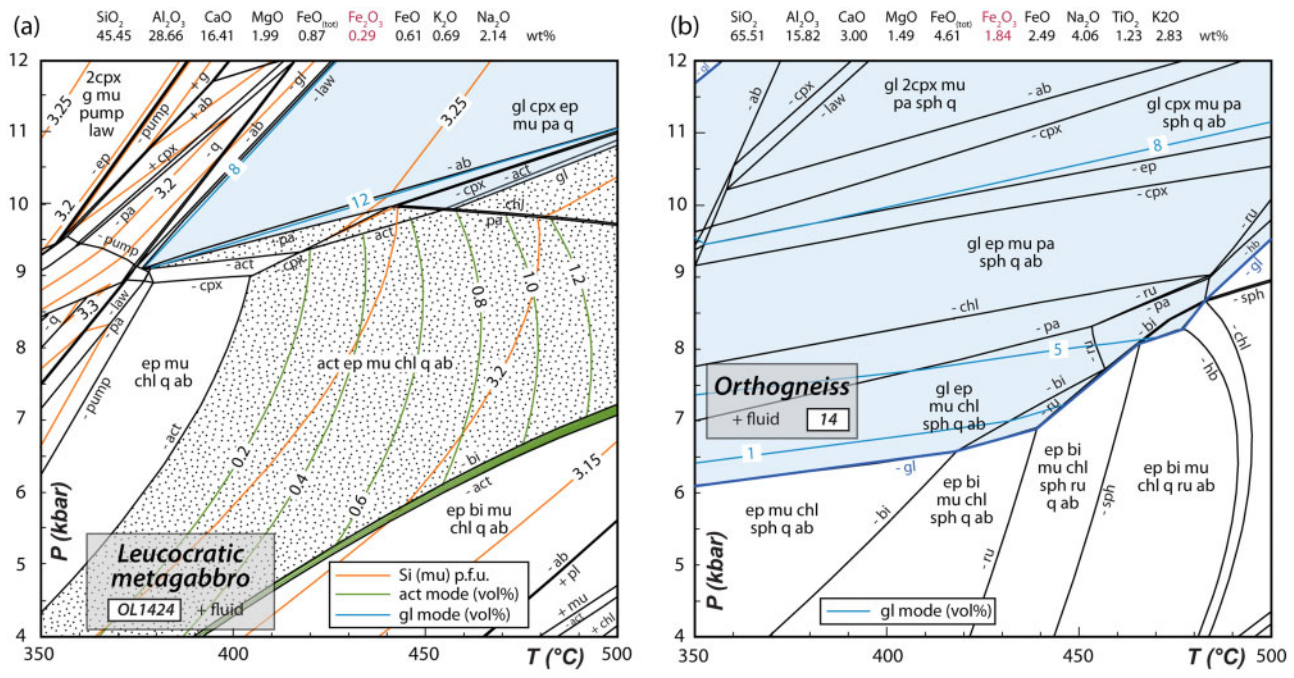



**Fig. 13.** *P*–*T* pseudosections for the leucocratic metagabbro OL1424 (a), and the orthogneiss 14 (b). The blue field indicates the *P*–*T* space where sodic amphibole ('gl') is stable. Blue lines show the glaucophane modal amount (vol%). The dotted field refers to the *P*–*T* space where actinolite is present. Diagram (a) is contoured (in green) for the actinolite modal amount (vol%). Muscovite compositional isopleths for Si (in p.f.u.) are reported in orange in (a). The amount of $Fe_2O_3$ used for the *P*–*T* calculation is indicated in red. The grey arrows indicate two possible *P*–*T* path consistent with mineral assemblages. For clarity, some fields are not labelled; their mineral assemblages can be deduced from assemblages in adjacent fields.

Downloaded from https://academic.oup.com/petrology/advance-article/doi/10.1093/petrology/egaa044/5810502 by guest on 29 September 2020

(Fig. 13b). In this field, sodic amphibole is modelled to be present from ~1 to ~5 vol% with increasing *P*. It is possible that the sample contained sodic amphibole and it has been replaced by chlorite–albite during decompression. Another explanation would be to accept as maximum *P*–*T* conditions at ~6·5 kbar and ~420 °C, which would explain the lack of sodic amphibole in the orthogneisses (Fig. 13b).

### *P*–*X*($Fe_2O_3$) modelling

*P*–*X*($Fe_2O_3$) pseudosections have been calculated for the different rock types at 450 °C to explore the effect of the oxidation state of the rock ($Fe^{3+}$–$Fe^{2+}$ ratio) on the stability of sodic amphibole and pyroxene. A *X*($Fe_2O_3$) range of 0·05–0·9 was considered, with *X*($Fe_2O_3$) = $Fe_2O_3$/FeO* [i.e. *X*($Fe_2O_3$) = 0 means that all Fe is bivalent; *X*($Fe_2O_3$) = 0·5 means that FeO and $Fe_2O_3$ are present in equal amounts]. The *P*–*X*($Fe_2O_3$) pseudosection (Fig. 14a) calculated at 450 °C for the hornblendite (OL02) shows that sodic amphibole is stable at relatively low $Fe_2O_3$ content above 7·5 kbar, whereas sodic pyroxene appears only at either very low (<0·14) or very high *X*($Fe_2O_3$) contents (0·60). Hematite and rutile are present only at high $Fe_2O_3$, whereas titanite is stable at low $Fe_2O_3$ content.

In the metatonalite (OL43), the stability field of sodic amphibole strongly varies with *X*($Fe_2O_3$) reaching the lowest *P* (~5·5 kbar) at a relatively low *X*($Fe_2O_3$) (~0·12; Fig. 14b). Below 5·5 kbar, the highest *X*($Fe_2O_3$) results in the appearance of hematite.

In the blueschist (VP7; Fig. 14c), hematite appears at relatively low *P* with increasing *X*($Fe_2O_3$) (>0·28). Sodic amphibole is stable at *P* > 7·5 kbar, except for very high *X*($Fe_2O_3$). From low to high *X*($Fe_2O_3$), sodic clinopyroxene is stable above ~9·5 kbar and ~6 kbar, and the composition varies from omphacite to aegirine, respectively. Above ~9 kbar, the two compositions coexist along a solvus in a narrow band at *X*($Fe_2O_3$) ~ 0·33 wt%. The mineral assemblage gl–g–ep–mu–q–sph–ab observed in the studied sample is stable between 7·5 and 9 kbar for a *X*($Fe_2O_3$) of 0·25–0·45 (i.e. lower than the $Fe^{3+}/Fe^{2+}$ ratio measured and used for the *P*–*T* calculation).

For the amphibole-gneiss (OL68B; Fig. 14d), the lowest *P* limit of sodic amphibole decreases from 8·5 to 7 kbar with increasing $Fe_2O_3$ content. Sodic amphibole disappears at *P* ≥ 10 kbar for *X*($Fe_2O_3$) ≥ 0·3. At relatively low *P*, hematite and a sodic pyroxene (aegirine) are present at high *X*($Fe_2O_3$) (>0·71).

In the pseudosection calculated for the leucocratic metagabbro (OL1424) at 450 °C (Fig. 15a), for the measured $Fe_2O_3$ value, the assemblage act–ep–mu–chl–q–ab is stable between 6·5 and 9·8 kbar. At these *P* conditions, an increase in the *X*($Fe_2O_3$) produces the disappearance of actinolite and an increase in the pistacite content of epidote. At *P* higher than 10 kbar, sodic amphibole and then sodic pyroxene (omphacite) appear. The calculated diagram indicates that the lower *P* stability limit of sodic amphibole is not dependent on the $Fe_2O_3$ content of the rock.

The *P*–*X*($Fe_2O_3$) pseudosection (Fig. 15b) calculated at 450 °C for the orthogneiss (14) shows that the lowest *P* limit of sodic amphibole first decreases from 9·2 to ~7 kbar with increasing *X*($Fe_2O_3$) (up to ~0·61). For *X*($Fe_2O_3$) higher than 0·61, the lowest *P* limit of sodic amphibole increases again up to ~8·5 kbar. Hematite is stable below 7 kbar at relatively high *X*($Fe_2O_3$) (>0·41). Above 10 kbar and high *X*($Fe_2O_3$), two pyroxenes (namely, aegirine and aegirine–augite) are stable.

In summary, although the stability field of sodic amphibole does depend on the oxidation state of the rock, the relation is not straightforward. In some lithologies, sodic amphibole is stabilized (at a given *T*) towards lower *P* at high $Fe^{3+}$/Fe* ratios (e.g. Fig. 14d), whereas in others the stability domain is maximized at low $Fe^{3+}$/Fe* ratios (e.g. Fig. 14b). In all lithologies, the chemistry of sodic amphibole, as calculated by the numerical model, displays an increasing $Fe^{3+}/(Fe^{3+} + Al^{3+})$ with increasing $Fe^{3+}$/Fe* ratio in the bulk composition (Fig. 15c). This variation is much less pronounced in the leucocratic metagabbro; that is, the rock with the lowest $Fe_2O_3$* and $Fe^{3+}$ contents, and the highest Mg#.

### *P*–$H_2O$ modelling

The previous calculations are based on the assumption that $H_2O$ was in excess during the metamorphic evolution. Here, we evaluate the possibility that metamorphism occurred under $H_2O$-undersaturated conditions. The aim of this modelling is to test if the absence of sodic amphibole in some rock types (e.g. in the orthogneiss and leucocratic metagabbro) can be linked to a limited $H_2O$ content in the system. The red lines in the calculated *P*–$H_2O$ pseudosections (Fig. 14d and Supplementary Data Figs S4 and S5) represent the $H_2O$–saturation surface and divide the diagrams in a $H_2O$-saturated (right) and a $H_2O$-undersaturated (left) part. All diagrams show that $H_2O$-undersaturation leads to important rapid variations of the stable mineral assemblages, including crystallization of minerals commonly not expected for a given rock type. In the bulk compositions investigated, at a given *T*, the minimum *P* of the stability field of sodic amphibole is generally rapidly displaced to higher *P* with increasing $H_2O$-undersaturation.

As an example, we detail here one sample (all samples are described in the Supplementary Data). A relatively large amount of $H_2O$ (~4–4·5 wt%, depending on *P*; Fig. 15d) is required to reach $H_2O$-saturated conditions in the hornblendite (OL02). With increasing $H_2O$-undersaturation, the minimum *P* of sodic amphibole stability first slightly decreases by ~0·5 kbar down to 8 kbar, then (for <3·4 wt% $H_2O$) rapidly increases up to >12 kbar (for <1·3 wt% $H_2O$). When $H_2O$-undersaturation is reached, the first changes of the mineral assemblages involve the disappearance of titanite, and the stabilization of rutile, hornblende and garnet over the entire *P* interval explored. Chloritoid appears at

Downloaded from https://academic.oup.com/petrology/advance-article/doi/10.1093/petrology/egaa044/5810502 by guest on 29 September 2020

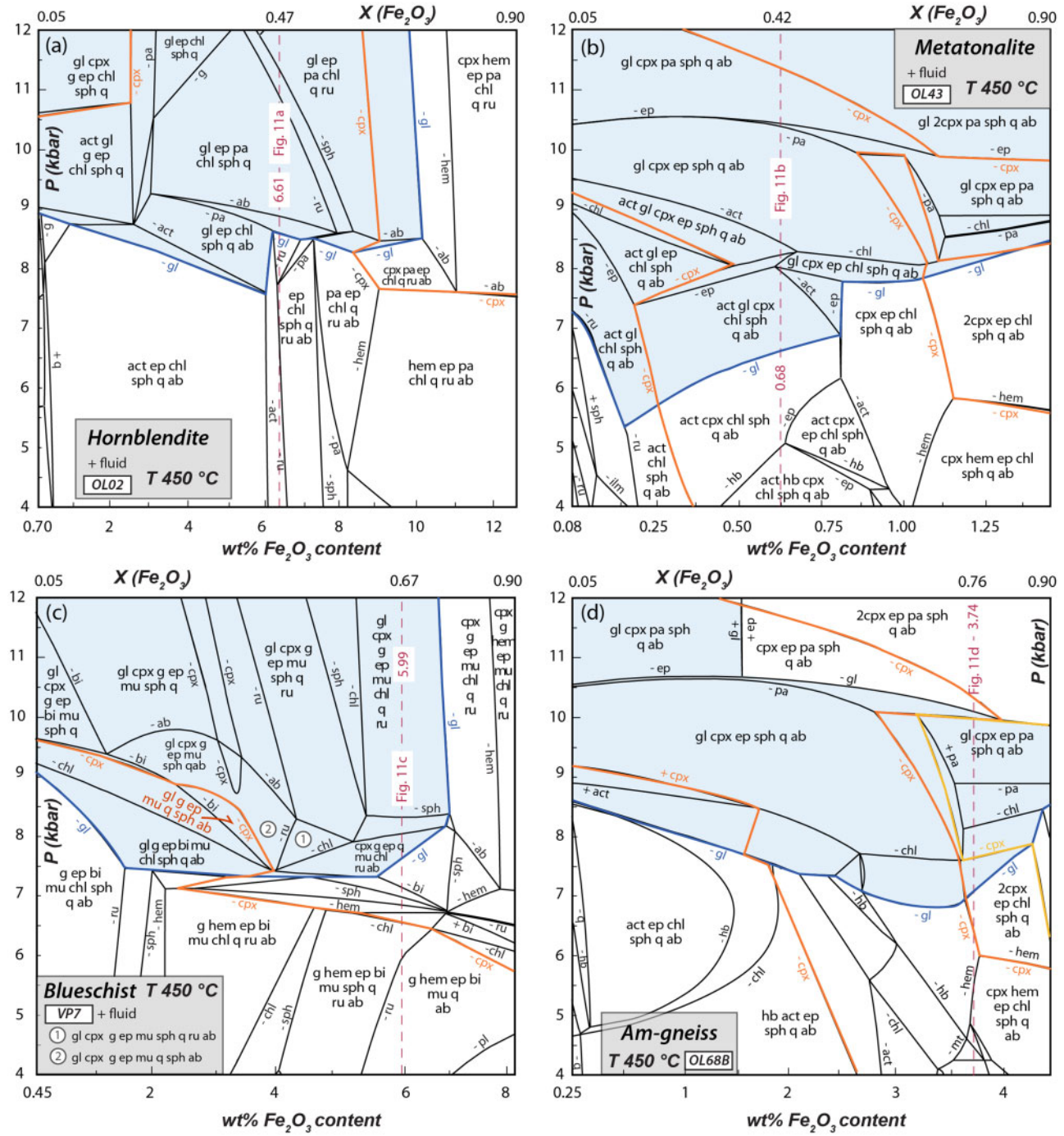



**Fig. 14.** *P*–*X*($Fe_2O_3$) pseudosections for the studied samples: (a) OL02, hornblendite; (b) OL43, metatonalite; (c) VP7, blueschist; (d) amphibole-gneiss (OL688). The blue field indicates the *P*–*T* space where sodic amphibole is stable. The red dashed line indicates the amount of $Fe_2O_3$ measured in the samples and used for the calculation of the *P*–*T* diagrams reported in Fig. 11. For clarity, some fields are not labelled; their mineral assemblages can be deduced from assemblages in adjacent fields.

$P > 8$ kbar, and staurolite for $P > 5{\cdot}5$ kbar at $H_2O$ ~1·6–2·6 wt%; kyanite becomes stable for $H_2O$ contents lower than ~3 wt% at 12 kbar and ~1·8 wt% at 4 kbar. These minerals have never been observed in the studied sample. Consequently, the $H_2O$-saturated pseudosection yields the best match between the model and petrological observations. As a whole, the *P*–$H_2O$ modelling (Fig. 14d and Figs S4 and S5) indicates that the assumption of excess water was probably valid for the studied rocks.

## Reliability of the thermodynamic modelling

Evaluating the limits of the thermodynamic modelling is a key issue for the interpretation of the rocks. Thermodynamic data on $Fe^{3+}$-rich blue amphibole and

Downloaded from https://academic.oup.com/petrology/advance-article/doi/10.1093/petrology/egaa044/5810502 by guest on 29 September 2020

sodic pyroxene are currently under development (Green *et al.*, 2016). Because few experimental data are available and because of the uncertainty of $Fe^{2+}/Fe^{3+}$ recalculation from microprobe analyses (as discussed above), these models may have a large degree of uncertainty. For this reason, we have carefully evaluated the match between calculated and analysed compositions of solid solution minerals and between observed and calculated parageneses in each studied sample (see above). Moreover, equilibrium conditions have not been reached in the described rocks as indicated by incompletely reacted relics (calcic amphiboles) and strong chemical zoning in blue amphibole and sodic pyroxene. This is expected during rather low-*T* metamorphism of magmatic rocks.

By essence, this work cannot evaluate the uncertainties associated with the end-member thermodynamic parameters and/or to the solid-solution models used, which are of the latest generation (Green *et al.*, 2016). For this, we should test a specific phase diagram assuming that *P*–*T* conditions are known, and compare the predictions of the phase diagram at such known *P*–*T* conditions in terms of mineral assemblage, modal proportion of the phase in this mineral assemblage, and phase chemistry (see, e.g. Forshaw *et al.*, 2019).

However, given the large number of phase diagrams we have calculated, some general inferences may be made. First, $H_2O$ saturation was most probably achieved in all studied samples, because of the lack of mineral phases (e.g. staurolite, kyanite, garnet, olivine, etc.) diagnostic of $H_2O$-undersaturated conditions, as predicted from the phase diagrams. Second, the influence of the $fO_2$ is fundamental but its exact relevance is difficult to assess, cumulating uncertainties in the determination of this ratio in the rock (our strategy gives the maximum amount of $Fe_2O_3$), and in the minerals from microprobe analyses (especially in amphibole; see above). By contrast, it is worth stressing that the composition of the pyroxene and amphibole, as calculated by the model, is in most cases similar to the one measured in our samples. When this composition is evolving with *P*–*T* conditions, the fit between calculated and observed composition is systematically in favour of the lower *P* range of stability for these minerals, giving some confidence in this approach.

## DISCUSSION

### Bulk-rock chemical control on the growth of sodic amphibole

Given the variety of rock types (from ultramafic to highly differentiated, felsic rocks) observed in the studied area, and the scarcity of rocks containing sodic amphibole and/or sodic pyroxene, the control of the bulk-rock chemistry on their occurrence should be carefully evaluated. Two groups of sodic amphibole-bearing rocks have been found. In a first group, the bulk-rock chemistry has not been significantly modified with respect to the protolith. In a second group, sodic amphibole develops in reaction zones at the contact between two contrasting lithologies; that is, in metasomatically altered rocks.

#### *Sodic amphibole in (nearly) isochemical rocks*

Sodic amphiboles (and sodic pyroxenes) may develop in a wide range of bulk-rock compositions, but are most commonly recorded in metabasites. In the studied area, metabasites constitute the bulk of the Berrio Gabbro. However, sodic amphibole is present only in the hornblendites, which differ from the other gabbros by having the lowest Mg# (61–67) (Fig. 9c). Therefore, the appearance of sodic amphiboles in this lithology may be primarily controlled by the more Fe-rich composition with respect the leucocratic and mesocratic gabbros (Mg# $>$ 80) where no sodic amphibole has been observed (Table 4; Fig. 9c).

The metatonalites have a very different composition from the hornblendites, being much richer in $Na_2O$ (Fig. 9c), and having a lower Fe* content. The appearance of sodic amphibole and sodic pyroxene may be therefore controlled by the high $Na_2O$ and low Mg#.

The blueschist displays very high Fe* content ($Fe_2O_3^* = 9{\cdot}09$ wt%), a high molar bulk $Fe^{3+}/Fe^*$ ratio (0·49) and a low Mg#, similar to the hornblendite. Therefore, the occurrence of sodic amphibole in this rock seems to be strongly controlled by its high Fe* content and $Fe^{3+}$ content.

#### *Sodic amphibole in reaction zones between granitic and ultramafic rocks*

The granitic orthogneisses in the studied area are devoid of sodic amphibole and/or sodic pyroxene. Amphibole-gneiss is found at the contact between the granitic orthogneiss and serpentinized ultramafic cumulate. The major element variation (e.g. Al, Mg, Na, K) between the granitic orthogneiss and the amphibole-gneiss demonstrates that the latter result from metasomatic processes at the contact between the two contrasting lithologies. With respect to the granitic orthogneiss, the amphibole-gneiss is enriched in CaO and $Na_2O$, and depleted in $K_2O$ (Fig. 9d). Trace elements display a decrease in LILE, whereas HFSE remains nearly constant. The depletion of LILE is explained by a decrease in muscovite abundance along the profile from the orthogneiss towards the amphibole-gneiss. The REE patterns of the orthogneiss and the amphibole-gneiss are similar. It should be noted that the protolith of the chlorite-schists is difficult to identify in the field, as nearby ultramafic rocks can be erroneously considered as their protoliths. However, the presence of magmatic zircon, apatite and minor allanite suggests a granitic protolith for the chlorite schists, which is supported by the similar REE patterns of the unaltered orthogneiss and the chlorite-schist. During the metasomatic alteration, granitoids may provide silica to the ultramafic cumulates, contributing to the formation of

Downloaded from https://academic.oup.com/petrology/advance-article/doi/10.1093/petrology/egaa044/5810502 by guest on 29 September 2020

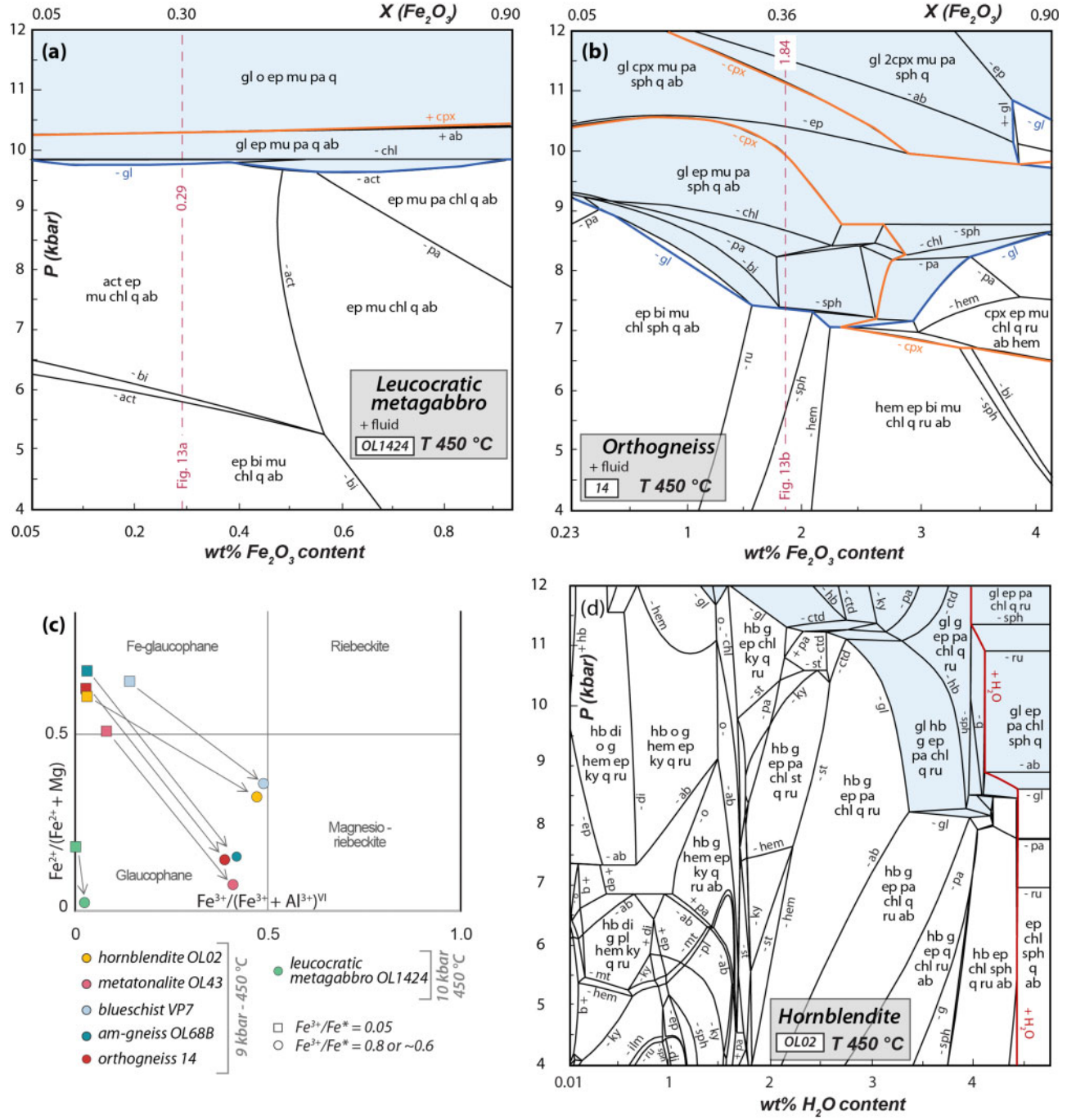



**Fig. 15.** *P–X*($Fe_2O_3$) pseudosection for (a) the leucocratic metagabbro (OL1424) and (b) Arolla orthogneiss (14). The blue field indicates the *P–T* space where sodic amphibole is stable. The red dashed line indicates the amount of $Fe_2O_3$ measured in the samples and used for the calculation of the *P–T* diagrams reported in Fig. 13. For clarity, some fields are not labelled; their mineral assemblages can be deduced from assemblages in adjacent fields. (c) Chemical composition of sodic amphibole as predicted by numerical modelling with the lowest and highest $Fe_2O_3$ content in the system. (d) *P–X* $H_2O$ pseudosections for the hornblendite (OL2). The red lines represent the $H_2O$-saturation surface and divide the diagram in an $H_2O$-saturated (right) and an $H_2O$-undersaturated (left) part.

talc veins in these rocks close to the contact with the granitoids (e.g. Jöns *et al.*, 2009). The preserved cumulate texture in the ultramafic rocks as well as the presence of porphyroclasts replaced by chlorite aggregates in the chlorite-schist suggest that intense deformation was very limited and strongly localized along the lithological contact.

## Metamorphic history of the Dent Blanche Tectonic System

In the DBTS, the Alpine evolution is heterogeneous, with large volumes preserving the pre-Alpine structures and parageneses. For example, paragneisses and amphibolites from the country-rocks of the Permian Mont Morion granitoid record pre-intrusive partial

Downloaded from https://academic.oup.com/petrology/advance-article/doi/10.1093/petrology/egaa044/5810502 by guest on 29 September 2020

melting at high $T$ (Manzotti *et al.*, 2018), but are devoid of any sign of Alpine metamorphism. Another example is provided by the Valpelline Series, in which Permian kilometre-scale high-grade paragneisses are preserved (Nicot, 1977; Gardien *et al.*, 1994; Manzotti & Zucali, 2013; Kunz *et al.*, 2018), except for rare kyanite at biotite–cordierite boundaries and chloritoid–muscovite pseudomorphs after cordierite (Kienast & Nicot, 1971).

In pervasively deformed rocks, the dominant synkinematic parageneses are ascribed to the greenschist facies. Above we discussed in detail the few lithologies in which sodic amphibole and sodic pyroxene have been found. Two different explanations can be envisaged for the sparse occurrence of these two index minerals.

1. Blueschist-facies metamorphism in the DBTS (i.e. well-developed blueschist-facies parageneses in all rocks that have been subjected to ductile deformation; Fig. 1) may have been present during an early stage of the Alpine compressional history, but has been extensively overprinted at greenschist facies during exhumation. As a consequence, the sodic amphiboles and sodic pyroxenes would represent relics of this early blueschist, only exceptionally preserved in some rocks.
2. According to the second hypothesis, peak $P$–$T$ conditions in the studied area never reached blueschist-facies conditions, but rather the transition between pumpellyite–actinolite or greenschist facies and blueschist facies (Fig. 1). In this $P$–$T$ domain, sodic amphibole and sodic pyroxene develop only in favourable chemical compositions; that is, in those especially rich in Na and $Fe^{3+}$ and/or displaying high $Fe^{2+}/(Fe^{2+} + Mg)$ ratios (low Mg#). At higher $P$, the range of bulk compositions susceptible to develop minerals diagnostic for the blueschist facies would have expanded, and their occurrence should have been much more common than observed.

Numerical modelling of the observed parageneses is consistent with a model in which all rocks containing sodic amphibole and sodic pyroxene developed at *c.* 400–450 °C (Figs 11 and 13), in the range of $8 \pm 1$ kbar. In this $P$–$T$ range, albite is stable in most lithologies, but Na would have been transferred from albite into sodic amphibole and/or sodic pyroxene in specific Na, Fe* and $Fe^{3+}$-rich bulk compositions. These characters may be 'primary' (as in the hornblendites), or be acquired following metasomatic transformations (as in the amphibole-gneiss). This would explain why sodic amphibole and sodic pyroxene are scarce in the entire DBTS.

An extensive greenschist-facies overprint cannot explain the actual distribution of the sodic amphiboles and pyroxenes for the following reasons.

1. In undeformed rocks, such as hornblendite in the gabbros, sodic amphibole mainly developed as a corona around the brown (magmatic) amphibole, a local domain with the highest Fe*. Away from the magmatic amphibole, in the plagioclase pseudomorphs, sodic amphibole is very rare, and actinolite is dominant. Therefore, the distribution of sodic amphibole in the undeformed rocks such as the hornblendites is not linked to a heterogeneous distribution of the greenschist-facies overprint, but to the local microchemical systems inherited from the magmatic protoliths.
2. In the amphibole-gneiss, field observations show that sodic amphibole is stable both during $D_1$, where aligned crystals of amphibole define the stretching lineation, and during or after $D_2$, where rosettes or sheaves grew across $D_2$ microfolds. In the orthogneiss protolith, sodic amphibole has not been observed. The continuity between the orthogneiss and the amphibole-gneiss can be ascertained thanks to the excellent and continuous outcrop conditions (Fig. 3) and both rocks must have shared the same $P$–$T$ history. The lack of sodic amphibole in the orthogneiss is therefore controlled by differences in bulk-rock chemistry, already present during the early metamorphic evolution of the DBTS.
3. The blueschists are interbedded with felsic gneisses. Both lithologies are folded together and share the deformational history ($D_1$, $D_2$), yet sodic amphibole is never present in the felsic gneisses, whereas it is common in the blueschists and apparently stable during both deformation events.

We thus conclude that pervasive greenschist-facies overprint cannot be the main controlling factor for the lack of sodic amphibole and pyroxene in most lithologies from the DBTS. Rather, bulk-rock chemical composition controls the growth of sodic amphibole in the most oxidized and/or the most Na- and Fe-rich rocks, pointing towards rather low $P$ ($\sim 8 \pm 1$ kbar) of equilibration of these assemblages.

## The greenschist- to blueschist-facies transition monitored by blue amphiboles

This study demonstrates, in the specific case of the Dent Blanche Tectonic System (Western Alps), the key role of bulk-rock chemistry [high $Na^+$, $Fe^{2+}/(Fe^{2+} + Mg)$ and $Fe^{3+}/Fe^*$] in stabilizing sodic amphibole and/or sodic pyroxene at relatively low $P$; that is, at the transition between the greenschist and the blueschist facies. Our calculations indicate that the chemical composition of sodic amphibole displays decreasing $Fe^{3+}/(Fe^{3+} + Al^{3+})$ ratios with increasing $P$ (for a given bulk-rock composition) and an increasing $Fe^{3+}/(Fe^{3+} + Al^{3+})$ with increasing $Fe^{3+}/Fe^*$ ratio in the bulk-rock.

To test these results further, the amphiboles from the Dent Blanche Tectonic System are compared with published analyses from other areas. Figure 16 represents a literature compilation of the chemical composition of sodic amphiboles from worldwide terrains at different metamorphic facies (i.e. $P$–$T$ conditions). The following groups have been made with reference to the

Downloaded from https://academic.oup.com/petrology/advance-article/doi/10.1093/petrology/egaa044/5810502 by guest on 29 September 2020

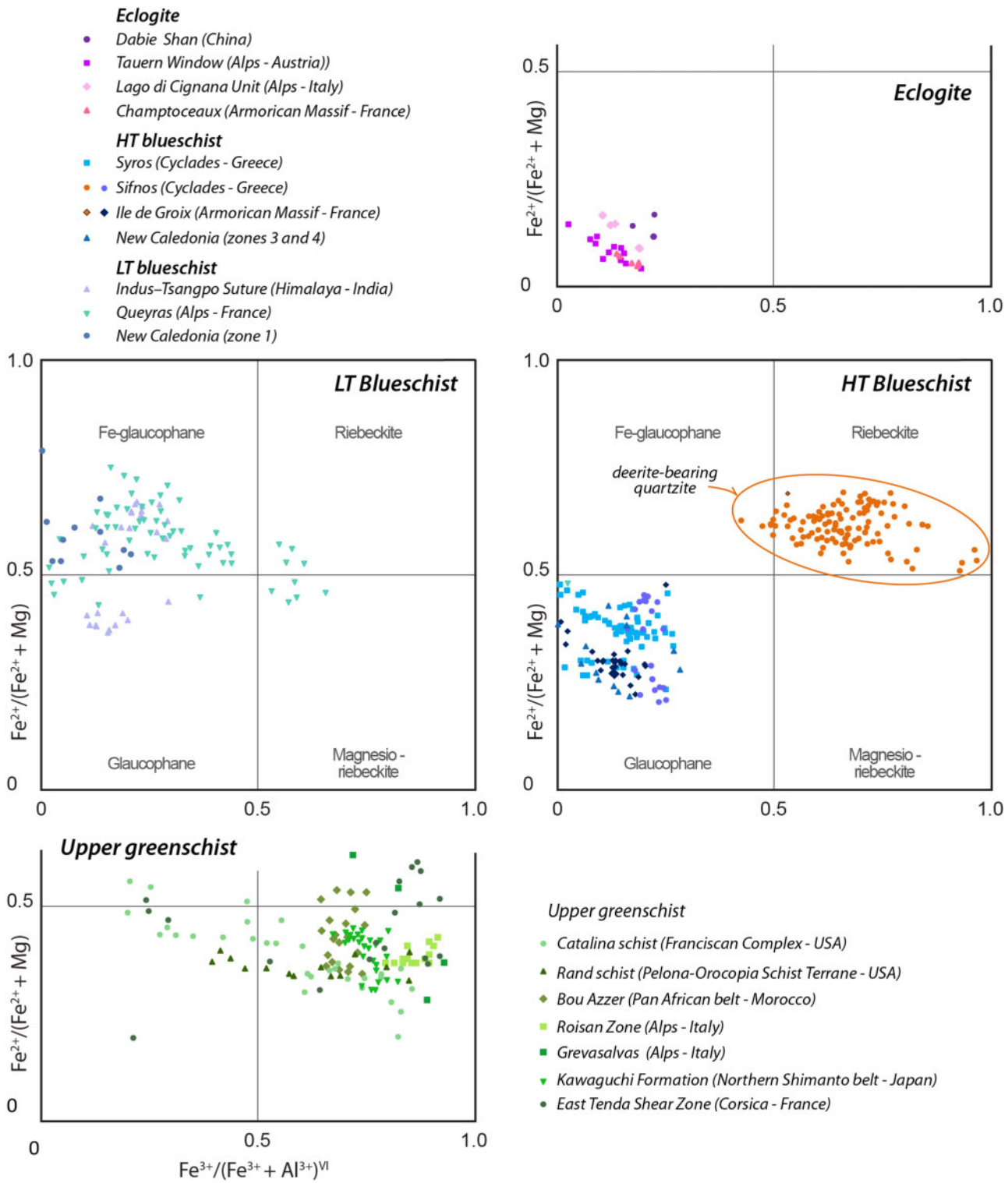



**Fig. 16.** Range of blueschist sodic amphiboles plotted in the Miyashiro & Banno (1958) diagram. The chemical composition of sodic amphibole has been recalculated following the procedure used in this study (see the section 'Mineral chemistry'). Upper greenschist: Catalina schist and Rand schist (Jacobson & Sorensen, 1986); Bou Azzer, Pan-African belt (Hefferan *et al.*, 2002; Bousquet *et al.*, 2008); Roisan Zone, Alps (Manzotti *et al.*, 2012); Grevasalvas, Alps (Philipp 1982); Kawaguchi Formation, Northern Shimanto belt (Aoki *et al.*, 2008); East Tenda Shear Zone, Corsica (Malasoma *et al.*, 2006; Maggi *et al.*, 2012; Rossetti *et al.*, 2015). Lower *T* blueschist: Indus–Tsangpo Suture, Himalaya (Groppo *et al.*, 2016); Queyras (Pognante & Kienast, 1989; Ballèvre & Lagabrielle, 1994); New Caledonia zone 1 (Clarke *et al.*, 1997; Fitzherbert *et al.*, 2003, 2005; Vitale Brovarone & Agard, 2013). Upper *T* blueschist: Syros (Schumacher *et al.*, 2008; Miller *et al.*, 2009; Philippon *et al.*, 2013; Skelton *et al.*, 2019); Sifnos (Evans, 1986; Groppo *et al.*, 2009*a*); Ile de Groix, Armorican Massif (Dudek & Kienast, 1989; Ballèvre *et al.*, 2003); New Caledonia zones 3 and 4 (Clarke *et al.*, 1997; Fitzherbert *et al.*, 2003, 2005; Vitale Brovarone & Agard, 2013; Taetz *et al.*, 2016). Eclogite: Dabie Shan (Zhang & Liou, 1994); Tauern Window, Alps (Holland, 1979); Lago di Cignana Unit, Alps (Groppo *et al.*, 2009*b*); Champtoceaux, Armorican Massif (M. Ballèvre, unpublished data).

Downloaded from https://academic.oup.com/petrology/advance-article/doi/10.1093/petrology/egaa044/5810502 by guest on 29 September 2020

parageneses observed in associated metabasites and metapelites.

Upper greenschist rocks are defined by the occurrence of high-Si muscovite and chlorite and the lack of biotite in metapelites. Most mafic rocks display assemblages consisting of albite, epidote, chlorite, actinolite and titanite. However, sodic amphibole and sodic pyroxene may be present in some lithologies, such as some metabasites and felsic orthogneisses (East Tenda Shear Zone: Malasoma *et al.*, 2006; Maggi *et al.*, 2012; Rossetti *et al.*, 2015), a few Mn- and Fe-rich metasediments (Roisan Zone: Ballèvre & Kienast, 1987; Manzotti *et al.*, 2012; Grevasalvas: Philipp, 1982), but their occurrence is always scarce. Reported sodic amphibole compositions from such terranes mainly plot in the Mg-riebeckite field, similar to the ones reported in this study.

The blueschist-facies occurrences have been subdivided into two groups. The low-*T* (LT) blueschists are distinguished by the common occurrence of lawsonite (rather than clinozoisite) in metabasites and the lack of garnet in associated metapelites (typically containing chlorite–chloritoid ± carpholite). Most sodic amphiboles in such terranes, such as the blueschists along the Indus–Tsangpo suture zone (Groppo *et al.*, 2016), those from the External domain of the Piemonte–Liguria Ocean (i.e. Queyras in Fig. 16) in the Western Alps (metagabbros: Pognante & Kienast, 1987; marbles: Ballèvre & Lagabrielle, 1994) or those from the New Caledonia (zone 1: Clarke *et al.*, 1997; Fitzherbert *et al.*, 2003, 2005; Vitale Brovarone & Agard, 2013) plot in the Fe-glaucophane field, whatever the composition of the bulk-rock in which they occur.

The high-*T* (HT) blueschists represent the bulk of glaucophane-bearing rocks, and are defined by the occurrence of garnet–chloritoid ± chlorite assemblages in the metapelites. Sodic amphibole is present in a large variety of bulk-rock compositions. These include the classic garnet-bearing blueschists, and glaucophane–epidote eclogites, derived from various kinds of metabasalts and metagabbros. Notable examples are found in the type locality for glaucophane Syros (Miller *et al.*, 2009; Philippon *et al.*, 2013; Skelton *et al.*, 2019), the Ile de Groix (Ballèvre *et al.*, 2003), and New Caledonia (zones 3 and 4, Clarke *et al.*, 1997; Fitzherbert *et al.*, 2003, 2005; Vitale Brovarone & Agard, 2013; Taetz *et al.*, 2016). In these localities, sodic amphibole is also present in some low-Al metapelites (e.g. Bosse *et al.*, 2002), a few marbles (e.g. Syros: Schumacher *et al.*, 2008), and the deerite-bearing rocks (Sifnos: Evans, 1986; Groppo *et al.*, 2009*a*), representing the most-Fe-rich rocks in this spectrum. Accordingly, the chemistry of sodic amphibole changes with bulk-rock composition but they all plot in the glaucophane field (except for the deerite-bearing parageneses).

Eclogite-facies occurrences are here defined when metabasites contain garnet–omphacite–kyanite and metapelites are equilibrated in the garnet–chloritoid–kyanite stability field (Tauern Window: Holland, 1979; Sesia Zone: Vuichard & Ballèvre, 1988) or at *T* above the stability field of chloritoid; that is, in the garnet–kyanite stability field (Champtoceaux: Ballèvre *et al.*, 1989). Sodic-amphibole parageneses in such rocks become very rare, and sodic amphibole displays the lowest $X\mathrm{Fe}^{2+}$ and $X\mathrm{Fe}^{3+}$ of the entire spectrum (glaucophane is therefore close to its end-member composition). In ultrahigh-*P* (UHP) terranes, sodic amphibole close to end-member glaucophane has been reported from the Dabie Shan (Zhang & Liou, 1994) and the Lago di Cignana (Groppo *et al.*, 2009*b*). In other UHP terranes, such as the Dora Maira Massif, sodic amphibole slightly departs from the glaucophane composition (e.g. Chopin, 1986; Kienast *et al.*, 1991; Schertl *et al.*, 1991).

This discussion shows that both the $\mathrm{Fe}^{3+}/(\mathrm{Fe}^{3+} + \mathrm{Al}^{3+})$ ratio and the $\mathrm{Fe}^{2+}/(\mathrm{Fe}^{2+} + \mathrm{Mg})$ of sodic amphibole decrease with increasing *P* and *T*. This general tendency is obviously counteracted by the effect of the bulk-rock composition, the best example being the deerite-bearing quartzites from Ile de Groix and Sifnos, which display much higher $\mathrm{Fe}^{3+}/(\mathrm{Fe}^{3+} + \mathrm{Al}^{3+})$ ratios than the other rock types from the same locality, although all were metamorphosed at high-*T* blueschist-facies conditions. The chemical composition of the sodic amphibole from the DBTS plots well in the diagram of the upper greenschist facies, again supporting the hypothesis that the bulk chemical composition controlled the growth of this mineral.

## CONCLUSIONS

1. In the DBTS sodic amphiboles and sodic pyroxenes have developed as a consequence of favourable whole-rock chemical composition, dominated by a combination of two or three parameters; namely, elevated $\mathrm{Na_2O}$ content, high $\mathrm{Fe}^{2+}/\mathrm{Fe}^{2+}\mathrm{Mg}$ and/or high $\mathrm{Fe}^{3+}$ content.
2. These parameters are achieved in specific rocks either because of their initial, pre-metamorphic chemistry (e.g. hornblendite, metatonalite), or because of some substantial metasomatic changes (amphibole-gneiss, a reaction zone at the boundary between felsic orthogneiss and ultramafic cumulates). Sodic amphiboles and pyroxenes develop only in the generally unreactive rocks of granitic bulk compositions where these are modified by metasomatic fluid–rock interactions in an open system.
3. Our thermodynamic modelling shows that the rocks may have equilibrated at 8 ± 1 kbar, 400–450 °C, with excess $\mathrm{H_2O}$. This study represents the first attempt to reconstruct the Alpine evolution of the DBTS by modelling the rare sodic amphibole- and sodic pyroxene-bearing rocks. Petrological models demonstrate that sodic amphibole and pyroxene formed in $\mathrm{Fe}^{3+}$-rich systems at relatively low *P* (∼8 ± 1 kbar, ∼450 °C); that is, at the transition from the greenschist- to the blueschist-facies metamorphism (path B

Downloaded from https://academic.oup.com/petrology/advance-article/doi/10.1093/petrology/egaa044/5810502 by guest on 29 September 2020

in Fig. 1). Therefore, these minerals record the incipient stages of HP–LT metamorphism fully developed in more internal units of the Sesia–Dent Blanche nappe stack.

4. Our conclusions are in line with the earlier studies of Miyashiro & Banno (1958) and Evans (1990). Indeed, thermodynamic modelling of specific bulk-rock compositions, using solid-solution models taking into account $Fe^{3+}$, indicates that the *P*–*T* stability field of sodic amphiboles is largely dependent on their chemical composition. This link has been substantiated by a compilation of the chemistry of sodic amphiboles in a large range of *P*–*T* conditions, displaying how the chemistry of sodic amphibole evolves with increasing metamorphic grade.

## ACKNOWLEDGEMENTS

We are grateful to Doug Tinkham for making available the conversion of the THERMOCALC mixing models for the Theriak-Domino software. We thank Chiara Groppo for providing us with the full dataset of amphibole analyses from the Indus–Tsangpo Suture (Ladakh, India) and from Sifnos (Greece). Nanfei Cheng and two anonymous reviewers are thanked for their constructive reviews. The editorial work of Reto Gieré and Marjorie Wilson has been highly appreciated.

## FUNDING

This work was financially supported by the Swiss National Science Foundation (Project PZ00P2_161202) and by the CNRS (AO-INSU 2017, TelluS Program).

## SUPPLEMENTARY DATA

Supplementary data are available at *Journal of Petrology* online.

## REFERENCES

Angiboust, S., Glodny, J., Oncken, O. & Chopin, C. (2014). In search of transient subduction interfaces in the Dent Blanche–Sesia Tectonic System (W. Alps). *Lithos* **205**, 298–321.

Aoki, K., Itaya, T., Shibuya, T., Masago, H., Kon, Y., Terabayashi, M., Kaneko, Y., Kawai, T. & Maruyama, S. (2008). The youngest blueschist belt in SW Japan: implication for the exhumation of the Cretaceous Sanbagawa high-*P*/*T* metamorphic belt. *Journal of Metamorphic Geology* **26**, 583–602.

Ayrton, S., Bugnon, C., Haarpainter, T., Weidmann, M. & Frank, E. (1982). Géologie du front de la nappe de la Dent Blanche dans la région des Monts-Dolins, Valais. *Eclogae Geologicae Helvetiae* **75**, 269–286.

Baletti, L., Zanoni, D., Spalla, M. I. & Gosso, G. (2012). Structural and petrographic map of the Sassa gabbro complex (Dent Blanche nappe, Austroalpine tectonic system, Western Alps, Italy. *Journal of Maps* **8**, 413–430.

Ballèvre, M. & Kienast, J. R. (1987). Découverte et signification de paragenèses à grenat amphibole bleue dans la couverture mésozoique de la nappe de la Dent-Blanche (Alpes Occidentales). *Comptes Rendus de l'Académie des Sciences, Série II* **305**, 43–46.

Ballèvre, M. & Lagabrielle, I. (1994). Garnet in blueschist-facies marbles from the Queyras unit (Western Alps): its occurrence and its significance. *Schweizerische Mineralogische und Petrographische Mitteilungen* **74**, 203–212.

Ballèvre, M., Pinardon, J.-L., Kiénast, J.-R. & Vuichard, J.-P. (1989). Reversal of Fe–Mg partitioning between garnet and staurolite in eclogite-facies metapelites from the Champtoceaux nappe (Brittany, France). *Journal of Petrology* **30**, 1321–1349.

Ballèvre, M., Pitra, P. & Bohn, M. (2003). Lawsonite growth in the epidote blueschists from Ile de Groix (Armorican Massif, France): a potential geobarometer. *Journal of Metamorphic Geology* **21**, 723–735.

Beltrando, M., Compagnoni, M. & Lombardo, B. (2010). (Ultra-) high pressure metamorphism and orogenesis: an alpine perspective. *Gondwana Research* **18**, 147–166.

Berger, A. & Bousquet, R. (2008). Subduction-related metamorphism in the Alps: review of isotopic ages based on petrology and their geodynamic consequences. In: Siegesmund, S., Fügenschuh, B. & Froitzheim, N. (eds) Tectonic Aspects of the Alpine-Dinaride- Carpathian System. *Geological Society, London, Special Publications* **298**, 117–144.

Bosse, V., Ballèvre, M. & Vidal, O. (2002). Ductile thrusting recorded by garnet isograd from blueschist-facies metapelites of the Ile de Groix, Armorican Massif, France. *Journal of Petrology* **43**, 485–510.

Bousquet, R., El Mamoun, R., Saddiqi, O., Goffé, B., Möller, A. & Madi, A. (2008). Mélanges and ophiolites during the Pan-African orogeny: the case of the Bou-Azzer ophiolite suite (Morocco). In: Ennih, N. & Liégeois, J.-P. (eds) The Boundaries of the West African Craton. *Geological Society, London, Special Publications* **297**, 233–247.

Bousquet, R., Oberhänsli, R., Schmid, S., Berger, A., Wiederkehr, M., Robert, C., Möller, A., Rosenberg, C., Zeilinger, G., Molli, G. & Koller, F. (2012). *Metamorphic framework of the Alps (1:1 000 000)*. Paris: Commission for the Geological Map of the World.

Bucher, K. & Grapes, R. (2011). *Petrogenesis of Metamorphic Rocks*. Berlin: Springer, 428 pp.

Brown, E. H. (1974). Comparison of the mineralogy and phase relations of blueschists from North Cascades, Washington, and greenschists from Otago. *Geological Society of America Bulletin* **85**, 333–344.

Brown, E. H. (1977). The crossite content of Ca-amphibole as a guide to pressure in metamorphism. *Journal of Petrology* **18**, 53–72.

Canepa, A., Castelletto, M., Cesare, B., Martin, S. & Zaggia, L. (1990). The Austroalpine Mont Mary nappe (Italian Western Alps). *Memorie di Scienze Geologiche* **42**, 1–17.

Carignan, J., Hild, P., Mevelle, G., Morel, J. & Yeghicheyan, D. (2001). Routine analyses of trace elements in geological samples using flow injection and low pressure on-line liquid chromatography coupled to ICP-MS: a study of geochemical reference materials, BR, DRN, UB-N, AN-G and GH. *Geostandards and Geoanalytical Research* **25**, 187–198.

Chopin, C. (1986). Phase relationships of ellenbergerite, a new high-pressure Mg–Al–Ti silicate in pyrope–coesite-quartzite from the Western Alps. In: Evans, W. E. & Brown, E. H. (eds) *Blueschists and Eclogites. Geological Society of America, Memoirs* **164**, 31–42.

Ciarapica, G., Passeri, L., Bonetto, F. & Dal Piaz, G. V. (2016). Facies and Late Triassic fossils in the Roisan zone,

Downloaded from https://academic.oup.com/petrology/advance-article/doi/10.1093/petrology/egaa044/5810502 by guest on 29 September 2020

Austroalpine Dent Blanche and Mt Mary–Cervino nappe system, NW Alps. *Swiss Journal of Geosciences* **109**, 69–81.

Clarke, G. L., Aitchison, J. C. & Cluzel, D. (1997). Eclogites and blueschists of the Pam Peninsula, NE New Caledonia: a reappraisal. *Journal of Petrology* **38**, 843–876.

Dal Piaz, G. V., Gianotti, F., Monopoli, B., Pennacchioni, G., Tartarotti, P. & Schiavo, A. (2010). *Note illustrative della Carta Geologica d'Italia alla scala 1:50.000. Foglio 091 Chatillon*. Rome: Servizio Geologico d'Italia, pp. 5–152.

Dal Piaz, G. V., Bistacchi, A., Gianotti, F., Monopoli, B. & Passeri, L. (2015). *Note illustrative della Carta Geologica d'Italia alla scala 1:50000*. Foglio 070 Cervino. Rome: Servizio Geologico d'Italia, pp. 1–431.

Dal Piaz, G. V., De Vecchi, G. & Hunziker, J. C. (1977). The Austroalpine layered gabbros of the Matterhorn and Mt. Collon–Dents de Bertol. *Schweizerische Mineralogische und Petrographische Mitteilungen* **57**, 59–88.

de Capitani, C. & Brown, T. H. (1987). The computation of chemical equilibrium in complex systems containing non-ideal solutions. *Geochimica et Cosmochimica Acta* **51**, 2639–2652.

de Capitani, C. & Petrakakis, K. (2010). The computation of equilibrium assemblage diagrams with Theriak/Domino software. *American Mineralogist* **95**, 1006–1016.

De Leo, S., Biino, G. & Compagnoni, R. (1987). Riequilibrazioni metamorfiche alpine nella serie di Valpelline e di Arolla a Nord di Bionaz (Valpelline–Aosta). *Rendiconti della Società Italiana di Mineralogia e Petrologia* **42**, 181–182.

Diehl, E. (1938). Geologisch-Petrographische Untersuchungen der Zone du Grand Combin im Val d'Ollomont. *Schweizerische Mineralogische und Petrographische Mitteilungen* **18**, 214–401.

Diehl, E. A., Masson, R. & Stutz, A. H. (1952). Contributo alla conoscenza del ricoprimento della Dent Blanche. *Memorie degli Istituti di Geologia e Mineralogia dell'Università di Padova* **17**, 1–52.

Diener, J. F. A. & Powell, R. (2010). Influence of ferric iron on the stability of mineral assemblages. *Journal of Metamorphic Geology* **28**, 599–613.

Diener, J. F. A., Powell, R., White, R. W. & Holland, T. J. B. (2007). A new thermodynamic model for clino- and orthoamphiboles in the system $Na_2O$–CaO–FeO–MgO–$Al_2O_3$–$SiO_2$–$H_2O$–O. *Journal of Metamorphic Geology* **25**, 631–656.

Dudek, K. & Kienast, J. R. (1989). Deerite from Ile de Groix, Brittany, France. *Mineralogical Magazine* **53**, 603–612.

Evans, W. E. (1986). Reactions among sodic, calcic, and ferromagnesian amphiboles, sodic pyroxene, and deerite in high-pressure metamorphosed ironstone, Siphnos, Greece. *American Mineralogist* **71**, 1118–1125.

Evans, B. W. (1990). Phase relations of epidote-blueschists. *Lithos* **25**, 3–23.

Evans, W. E. & Brown, E. H. (eds) (1986). *Blueschists and Eclogites. Geological Society of America, Memoirs* **164**, 423 pp.

Fitzherbert, J. A., Clarke, G. L. & Powell, R. (2003). Lawsonite–omphacite-bearing metabasites of the Pam Peninsula, NE New Caledonia: evidence for disrupted blueschist- to eclogite-facies conditions. *Journal of Petrology* **44**, 1805–1831.

Fitzherbert, J. A., Clarke, G. L. & Powell, R. (2005). Preferential retrogression of high-*P* metasediments and the preservation of blueschist to eclogite facies metabasite during exhumation, Diahot terrane, NE New Caledonia. *Lithos* **83**, 67–96.

Forshaw, J. B., Waters, D. J., Pattison, R. M., Palin, R. M. & Gopon, P. (2019). A comparison of observed and thermodynamically predicted phase equilibria and mineral compositions in mafic granulites. *Journal of Metamorphic Geology* **37**, 153–179.

Gardien, V., Reusser, E. & Marquer, D. (1994). Pre-Alpine metamorphic evolution of the gneisses from Valpelline series (Western Alps, Italy). *Schweizerische Mineralogische und Petrographische Mitteilungen* **74**, 489–502.

Green, E. C. R., White, R. W., Diener, J. F. A., Powell, R., Holland, T. J. B. & Palin, R. M. (2016). Activity–composition relations for the calculation of partial melting equilibria in metabasic rocks. *Journal of Metamorphic Geology* **34**, 845–869.

Groppo, C., Beltrando, M. & Compagnoni, R. (2009b). The *P*–*T* of the ultra-high pressure Lago di Cignana and adjoining high-pressure meta-ophiolitic units: insights into the evolution of the subducting Tethyan slab. *Journal of Metamorphic Geology* **27**, 207–231.

Groppo, C., Forster, M., Lister, G. & Compagnoni, R. (2009a). Glaucophane schists and associated rocks from Sifnos (Cyclades, Greece). *Lithos* **109**, 254–273.

Groppo, C., Rolfo, F., Sachan, H. K. & Rai, S. K. (2016). Petrology of blueschist from the Western Himalaya (Ladakh, NW India): exploring the complex behavior of a lawsonite-bearing system in a paleo-accretionary setting. *Lithos* **252–253**, 41–56.

Haggert, S. E. (1991). Oxide textures—a mini atlas. In: Lindsley, D. H. (ed.) *Oxide Minerals: Petrologic and Magnetic Significance.* Mineralogical Society of America, Reviews in Mineralogy **25**, 129–219.

Handy, M. R., Schmid, S. M., Bousquet, R., Kissling, E. & Bernoulli, D. (2010). Reconciling plate-tectonic reconstructions of Alpine Tethys with the geological–geophysical record of spreading and subduction in the Alps. *Earth-Science Reviews* **102**, 121–168.

Hefferan, K. P., Admou, H., Hilal, R., Karson, J. A., Saquaque, A., Juteau, T., Bohn, M. M., Samson, S. D. & Kornprobst, J. M. (2002). Proterozoic blueschist-bearing mélange in the Anti-Atlas Mountains, Morocco. *Precambrian Research* **118**, 179–194.

Holland, T. J. B. (1979). High water activties in the generation of high pressure kyanite eclogites of the Tauern Window. *Journal of Geology* **87**, 1–27.

Holland, T. & Powell, R. (2003). Activity–composition relations for phases in petrological calculations; an asymmetric multicomponent formulation. *Contributions to Mineralogy and Petrology* **145**, 492–501.

Holland, T. J. B. & Powell, R. (2011). An improved and extended internally consistent thermodynamic dataset for phases of petrological interest, involving a new equation of state for solids. *Journal of Metamorphic Geology* **29**, 333–383.

Jacobson, C. E. & Sorensen, S. S. (1986). Amphibole compositions and metamorphic history of the Rand Schist and the greenschist unit of the Catalina Schist, Southern California. *Contributions to Mineralogy and Petrology* **92**, 308–315.

Jöns, N., Bach, W. & Schroeder, T. (2009). Formation and alteration of plagiogranites in an ultramafic-hosted detachment fault at Mid-Atlantic Ridge (ODP Leg 209). *Contributions to Mineralogy and Petrology* **157**, 625–639.

Kienast, J.-R., Lombardo, B., Biino, G. & Pinardon, J.-L. (1991). Petrology of very-high-pressure eclogitic rocks from the Brossasco–Isasca Complex, Dora–Maira Massif, Italian Western Alps. *Journal of Metamorphic Geology* **9**, 19–34.

Kienast, J. R. & Nicot, E. (1971). Présence d'une paragenèse à disthène et chloritoïde (d'âge alpin probable) dans les gneiss à sillimanite, grenat et cordiérite de Valpelline (Val d'Aoste, Italie). *Comptes Rendus de l'Académie des Sciences* **D-272**, 1836–1840.

Kirst, F. (2017). Polyphase greenschist-facies reactivation of the Dent Blanche Basal Thrust (Western Alps) during

Downloaded from https://academic.oup.com/petrology/advance-article/doi/10.1093/petrology/egaa044/5810502 by guest on 29 September 2020

progressive Alpine orogeny. *Swiss Journal of Geosciences* **110**, 503–521.

Kunz, B. E., Manzotti, P., von Niederhäusern, B., Engi, M., Darling, J. R., Giuntoli, F. & Lanari, P. (2018). Permian high-temperature metamorphism in the Western Alps (MW Italy). *International Journal of Earth Sciences* **107**, 203–229.

Leake, B. E., Woolley, A. R., Arps, C. E. S., Birch, W. D., Gilbert, M. C., Grice, J. D. & Guo, Y. Z. (1997). Nomenclature of amphiboles: report of the subcommittee on amphiboles of the International Mineralogical Association, commission on new minerals and mineral names. *American Mineralogist* **82**, 1019–1037.

Le Maître, R. W. (2002). *Igneous Rocks—a Classification and Glossary of Terms, Recommendations of the IUGS Subcommission on the Systematics of Igneous Rocks*, 2nd edn. Cambridge: Cambridge University Press.

Liou, J. G., Maruyama, S. & Cho, M. (1985). Phase equilibria and mineral paragensis in low-grade metamorphism. *Mineralogical Magazine* **49**, 321–333.

López-Carmona, A., Pitra, P. & Abati, J. (2013). Blueschist-facies metapelites from the Malpica–Tui Unit (NW Iberian Massif): phase equilibria modelling and $H_2O$ and $Fe_2O_3$ influence in high-pressure assemblages. *Journal of Metamorphic Geology* **31**, 263–280.

Maggi, M., Rossetti, F., Corfu, F., Theye, T., Andersen, T. B. & Faccenna, C. (2012). Clinopyroxene–rutile phyllonites from the East Tenda Shear Zone (Alpine Corsica, France): pressure–temperature–time constraints to the Alpine reworking of Variscan Corsica. *Journal of the Geological Society, London* **169**, 723–732.

Malasoma, A., Marroni, M., Musumeci, G. & Pandolfi, L. (2006). High-pressure mineral assemblage in granitic rocks from continental units, Alpine Corsica, France. *Geological Journal* **41**, 49–59.

Manzotti, P. (2011). Petro-structural map of the Dent Blanche tectonic system between Valpelline and Valtournenche valleys, Western Italian Alps—1:20 000, 1:10 000, 1:2500. *Journal of Maps* **7**, 340–352.

Manzotti, P. & Ballèvre, M. (2017). Tectonic history of the Dent Blanche. *Geological Field Trips* **9**, 1–73.

Manzotti, P., Ballèvre, M. & Dal Piaz, G. V. (2017). Continental gabbros in the Dent Blanche Tectonic System (Western Alps): from the pre-Alpine crustal structure of the Adriatic palaeomargin to the geometry of an alleged subduction interface. *Journal of the Geological Society, London* **174**, 541–556.

Manzotti, P., Ballèvre, M., Zucali, M., Robyr, M. & Engi, M. (2014b). The tectonometamorphic evolution of the Sesia–Dent Blanche nappes (internal Western Alps): review and synthesis. *Swiss Journal of Geosciences* **107**, 309–336.

Manzotti, P., Rubatto, D., Darling, J., Zucali, M., Cenki-Tok, B. & Engi, M. (2012). From Permo-Triassic lithospheric thinning to Jurassic rifting at the Adriatic margin: petrological and geochronological record in Valtournenche (Western Italian Alps). *Lithos* **146–147**, 276–292.

Manzotti, P., Rubatto, D., Zucali, M., El Korh, A., Cenki-Tok, B., Ballèvre, M. & Engi, M. (2018). Permian magmatism and metamorphism in the Dent Blanche nappe: constraints from field observations and geochronology. *Swiss Journal of Geosciences* **111**, 79–97.

Manzotti, P. & Zucali, M. (2013). The pre-Alpine tectonic history of the Austroalpine continental basement in the Valpelline unit (Western Italian Alps). *Geological Magazine* **150**, 153–172.

Manzotti, P., Zucali, M., Ballèvre, M., Robyr, M. & Engi, M. (2014a). Geometry and kinematics of the Roisan–Cignana Shear Zone, and the orogenic evolution of the Dent Blanche Tectonic System (Western Alps). *Swiss Journal of Geosciences* **107**, 23–47.

Maruyama, S., Cho, M. & Liou, J. G. (1986). Experimental investigations of blueschist–greenschist transition equilibria: pressure dependence of $Al_2O_3$ content in sodic amphiboles—a new geobarometer. In: Evans, W. E. & Brown, E. H. (eds) *Blueschists and Eclogites. Geological Society of America, Memoirs. Geological Society of America Bulletin* **164**, 1–16.

Miller, D. P., Marschall, H. R. & Schumacher, J. C. (2009). Metasomatic formation and petrology of blueschist-facies hybrid rocks from Syros (Greece): implications for reactions at the slab–mantle interface. *Lithos* **107**, 53–67.

Miyashiro, A. & Banno, S. (1958). Nature of glaucophanic metamorphism. *American Journal of Science* **256**, 97–110.

Monjoie, P., Bussy, F., Schaltegger, U., Mulch, A., Lapierre, H. & Pfeifer, H. R. (2007). Contrasting magma types and timing of intrusion in the Permian layered mafic complex of Mont Collon (Western Alps, Valais, Switzerland). *Swiss Journal of Geosciences* **100**, 125–135.

Müntener, O., Manatschal, G., Desmurs, L. & Pettke, T. (2010). Plagioclase peridotites in ocean–continent transitions: refertilized mantle domains generated by melt stagnation in the shallow mantle lithosphere. *Journal of Petrology* **51**, 255–294.

Nicot, E. (1977). Les roches méso- et catazonales de la Valpelline (nappe de la Dent Blanche, Alpes Italiennes). PhD dissertation, Université de Paris.

Oberhänsli, R., Bousquet, R. & Engi, M. (2004). *Metamorphic Structure of the Alps*, 1st edn. Paris: Commission for the Geological Map of the World (CCGM/CGMW).

Okay, A. I. (1980). Sodic amphiboles as oxygen fugacity indicators in metamorphism. *Journal of Geology* **88**, 225–232.

Pennacchioni, G. & Guermani, A. (1993). The mylonites of the Austroalpine Dent Blanche nappe along the northwestern side of the Valpelline Valley (Italian Western Alps). *Memorie di Scienze Geologiche* **45**, 37–55.

Philipp, R. (1982). Die Alkaliamphibole der Platta-Decke zwischen Silsersee und Lunghinpass (Graubünden). *Schweizerische Mineralogische und Petrographische Mitteilungen* **62**, 437–455.

Philippon, M., Gueydan, F., Pitra, P. & Brun, J.-P. (2013). Preservation of subducted-related prograde deformation in lawsonite pseudomorph-bearing rocks. *Journal of Metamorphic Geology* **31**, 571–583.

Pognante, U. & Kienast, J.-R. (1987). Blueschist and eclogite transformations in Fe–Ti gabbros: a case from the Western Alps ophiolites. *Journal of Petrology* **28**, 271–292.

Roda, M. & Zucali, M. (2008). Meso and microstructural evolution of the Mont Morion metaintrusives complex (Dent Blanche nappe, Austroalpine domain, Valpelline, Western Italian Alps). *Italian Journal of Geosciences* **127**, 105–123.

Rossetti, F., Glodny, J., Theye, T. & Maggi, M. (2015). Pressure–temperature–deformation–time of the ductile Alpine shearing in Corsica: from orogenic construction to collapse. *Lithos* **218–219**, 99–116.

Schertl, H.-P., Schreyer, W. & Chopin, C. (1991). The pyrope–coesite rocks and their country rocks at Parigi, Dora Maira Massif, Western Alps: detailed petrography, mineral chemistry and *P–T* path. *Contributions to Mineralogy and Petrology* **108**, 1–21.

Schumacher, J. C. (1997). The estimation of ferric iron in electron microprobe analysis of amphiboles. *American Mineralogist* **82**, 643–651.

Schumacher, J. C. (2007). Metamorphic amphiboles: composition and coexistence. In: Hawthorne, F. C., Oberti, R., Della Ventura, G. & Mottana, A. (eds) Amphiboles: crystal,

Downloaded from https://academic.oup.com/petrology/advance-article/doi/10.1093/petrology/egaa044/5810502 by guest on 29 September 2020

chemistry, occurrence, and health issues. Mineralogical Society of America and Geochemical Society, Reviews in Mineralogy and Geochemistry **67**, 359–416.

Schumacher, J. C., Brady, J. B., Cheney, J. T. & Tonnsen, R. R. (2008). Glaucophane-bearing marbles on Syros, Greece. *Journal of Petrology* **49**, 1667–1686.

Schmid, S. M., Fügenschuh, B., Kissling, E. & Schuster, R. (2004). Tectonic map and overall architecture of the Alpine orogen. *Eclogae Geologicae Helvetiae* **97**, 93–117.

Skelton, A., Peillod, A., Glodny, J., Klonowska, I., Månbro, C., Lodin, K. & Ring, U. (2019). Preservation of high-*P* rocks coupled to rock composition and the absence of metamorphic fluids. *Journal of Metamorphic Geology* **37**, 359–381.

Stutz, A. H. (1940). Die Gesteine der Arollaserie im Valpelline (Provinz Aosta, Oberitalien). *Schweizerische Mineralogische und Petrographische Mitteilungen* **20**, 118–246.

Sun, S. S. & McDonough, W. F. (1989). Chemical and isotopic systematics of oceanic basalts: implications for mantle composition and processes. In: Saunders, A. D. & Norry, M. J. (eds) *Magmatism in Ocean Basins. Geological Society*, London, Special Publications **42**, 313–345.

Taetz, S., John, T., Bröcker, M. & Spandler, C. (2016). Fluid–rock interaction and evolution of a high-pressure/low-temperature vein system in eclogite from New Caledonia: insights into intraslab fluid flow processes. *Contributions to Mineralogy and Petrology* **171**, 90.

Vitale Brovarone, A. & Agard, A. (2013). True metamorphic isograds or tectonically sliced metamorphic sequence? New high-spatial resolution petrological data for the New Caledonia case study. *Contributions to Mineralogy and Petrology* **166**, 451–469.

Vuichard, J.-P. & Ballèvre, M. (1988). Garnet–chloritoid equilibria in eclogitic pelitic rocks from the Sesia Zone (Western Alps), their bearing on phase relations in high pressure metapelites. *Journal of Metamorphic Geology* **6**, 135–157.

Warren, C. J. & Waters, D. J. (2006). Oxidized eclogites and garnet blueschists from Oman: *P–T* path modelling in the NCFMASHO system. *Journal of Metamorphic Geology* **24**, 783–802.

Wei, C. J. & Powell, R. (2004). Calculated phase relations in high-pressure metapelites in the system NKFMASH ($Na_2O$–$K_2O$–FeO–MgO–$Al_2O_3$–$SiO_2$–$H_2O$). *Journal of Petrology* **45**, 183–202.

Weidmann, M. & Zaninetti, L. (1974). Quelques données sur la série du Mont-Dolin (nappe de la Dent-Blanche, Valais). *Eclogae Geologicae Helvetiae* **67**, 597–603.

White, R. W., Powell, R., Holland, T. J. B. & Worley, B. A. (2000). The effect of $TiO_2$ and $Fe_2O_3$ on metapelitic assemblages at greenschist and amphibolite facies conditions: mineral equilibria calculations in the system $K_2O$-FeO-MgO-$Al_2O_3$-$SiO_2$-$H_2O$-$TiO_2$-$Fe_2O_3$. *Journal of Metamorphic Geology* **18**, 497–511.

White, R. W., Powell, R. & Clarke, G. L. (2002). The interpretation of reaction textures in Fe-rich metapelitic granulites of the Musgrave Block, central Australia: constraints from mineral equilibria calculations in the system $K_2O$–FeO–MgO–$Al_2O_3$–$SiO_2$–$H_2O$–$TiO_2$–$Fe_2O_3$. *Journal of Metamorphic Geology* **20**, 41–55.

White, R. W., Powell, R., Holland, T. J. B., Johnson, T. E. & Green, E. C. R. (2014b). New mineral activity–composition relations for thermodynamic calculations in metapelitic systems. *Journal of Metamorphic Geology* **32**, 261–286.

White, R. W., Powell, R. & Johnson, T. E. (2014a). The effect of Mn on mineral stability in metapelites revisited: new *a–x* relations for manganese-bearing minerals. *Journal of Metamorphic Geology* **32**, 809–828.

Winchester, J. A. & Floyd, P. A. (1977). Geochemical discrimination of different magma series and their differentiation products using immobile elements. *Chemical Geology* **20**, 325–343.

Zhang, R.-Y. & Liou, J. G. (1994). Coesite-bearing eclogite in Henan Province, central China: detailed petrography, glaucophane stability and *PT*-path. *European Journal of Mineralogy* **6**, 217–233.

Downloaded from https://academic.oup.com/petrology/advance-article/doi/10.1093/petrology/egaa044/5810502 by guest on 29 September 2020